

RESEARCH ARTICLE



The structural logic of dynamic signaling in the *Escherichia coli* serine chemoreceptor

Georgina I. Reyes | Caralyn E. Flack | John S. Parkinson 

School of Biological Sciences, University of Utah, Salt Lake City, Utah, USA

Correspondence

John S. Parkinson, School of Biological Sciences, University of Utah, 257 South 1400 East, Salt Lake City, UT 84112, USA.
Email: parkinson@biology.utah.edu

Funding information

National Institute of General Medical Sciences, Grant/Award Number: GM19559; Scott A. Lloyd Memorial Graduate Fellowship at the University of Utah; National Cancer Institute, Grant/Award Number: CA42014

Review Editor: John Kuriyan

Abstract

The experimental challenges posed by integral membrane proteins hinder molecular understanding of transmembrane signaling mechanisms. Here, we exploited protein crosslinking assays in living cells to follow conformational and dynamic stimulus signals in Tsr, the *Escherichia coli* serine chemoreceptor. Tsr mediates serine chemotaxis by integrating transmembrane serine-binding inputs with adaptational modifications of a methylation helix bundle to regulate a signaling kinase at the cytoplasmic tip of the receptor molecule. We created cysteine replacements at Tsr residues adjacent to hydrophobic packing faces of the bundle helices and crosslinked them with a cell-permeable, bifunctional thiol-reagent. We identified an extensively crosslinked dynamic junction midway through the methylation helix bundle that seemed uniquely poised to respond to serine signals. We explored its role in mediating signaling shifts between different packing arrangements of the bundle helices by measuring crosslinking in receptor molecules with apposed pairs of cysteine reporters in each subunit and assessing their signaling behaviors with an *in vivo* kinase assay. In the absence of serine, the bundle helices evinced compact kinase-ON packing arrangements; in the presence of serine, the dynamic junction destabilized adjacent bundle segments and shifted the bundle to an expanded, less stable kinase-OFF helix-packing arrangement. AlphaFold models of kinase-active Tsr showed a prominent bulge and kink at the dynamic junction that might antagonize stable structure at the receptor tip. Serine stimuli might inhibit kinase activity by shifting the bundle to a less stably-packed conformation that relaxes structural strain at the receptor tip, thereby allowing it to stabilize and freeze kinase activity.

KEYWORDS

4-helix bundle, bacterial chemotaxis, *in vivo* crosslinking, sensory transduction

This is an open access article under the terms of the [Creative Commons Attribution-NonCommercial-NoDerivs](https://creativecommons.org/licenses/by-nc-nd/4.0/) License, which permits use and distribution in any medium, provided the original work is properly cited, the use is non-commercial and no modifications or adaptations are made.

© 2024 The Author(s). *Protein Science* published by Wiley Periodicals LLC on behalf of The Protein Society.

1 | INTRODUCTION

The chemotaxis machinery of *Escherichia coli* has long provided a powerful experimental system for investigating molecular mechanisms of stimulus detection and signaling by transmembrane chemoreceptors (Bi and Sourjik 2018; Colin et al. 2021; Parkinson et al. 2015). The best understood bacterial chemoreceptors belong to the methyl-accepting chemotaxis protein (MCP) superfamily (Wuichet and Zhulin 2010). MCP molecules are homodimeric, mainly alpha-helical proteins that assemble signaling complexes at their cytoplasmic hairpin tips through interactions with two soluble partner proteins, a histidine autokinase (CheA) and a scaffolding protein (CheW) that couples CheA activity to chemoreceptor control (Figures 1a and S1, Supporting Information). The fundamental unit of chemoreceptor activity is a core signaling unit comprising six receptor molecules organized as two trimers of dimers, one CheA homodimer, and two CheW protomers (Li and Hazelbauer 2011) (Figure S1). These signaling complexes are in turn networked into large cooperative signaling arrays through hexameric CheA-CheW and CheW-CheW rings (Pinas et al. 2016, 2022).

Much of what we know about the molecular mechanisms of MCP signaling has come from studies of the *E. coli* Tsr (serine) and Tar (aspartate) chemoreceptors. In isotropic chemical environments, Tsr and Tar activate their CheA partners, which autophosphorylate using ATP, then donate their phosphoryl groups to the CheY response regulator (reviewed in Parkinson et al. 2015). Phospho-CheY molecules interact with flagellar basal bodies to initiate directional changes that produce a random-walk swimming pattern. Upon sensing an attractant increase, Tsr and Tar inhibit CheA, halting the flux of phosphoryl groups to CheY to promote forward swimming, the default motor behavior. Cellular phospho-CheY is short-lived due to the action of a dedicated phosphatase (CheZ), thereby ensuring rapid behavioral responses to chemoeffector stimuli.

A sensory adaptation system modulates the ligand sensitivity of the Tsr and Tar kinase control responses, enabling swimming cells to detect spatial chemoeffector gradients in temporal fashion by comparing current chemical conditions with those averaged over the past few seconds of their travels (reviewed in Parkinson et al. 2015). Two MCP-specific enzymes, CheR, a methyltransferase, and CheB, a methyl-esterase, respectively methylate or demethylate glutamyl residues in the cytoplasmic portion of the receptor molecule to adjust its signaling activity to prevailing chemoeffector levels. Under steady-state conditions, CheB demethylates receptors in the kinase-ON state and shifts them toward kinase-OFF output, whereas CheR methylates receptor molecules in

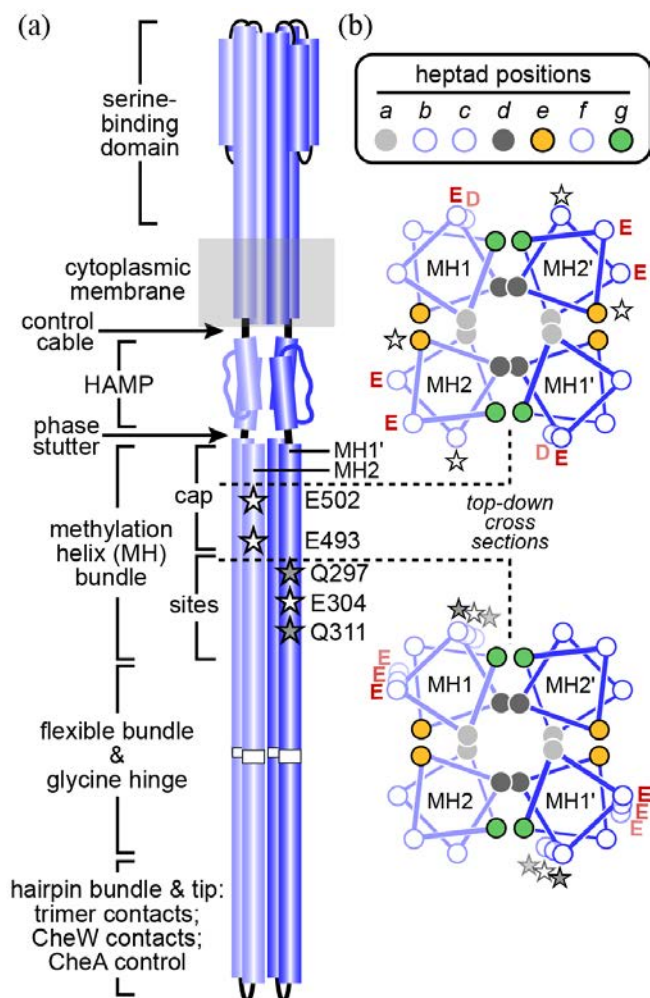


FIGURE 1 Tsr structural features. (a) Signaling elements in the Tsr homodimer. Cylinders represent alpha-helical segments of Tsr subunits (light and dark blue), drawn approximately to scale. The cytoplasmic segment below the HAMP domain is an antiparallel, 4-helix bundle. Stars indicate adaptational modification site residues, E (white) and Q (gray). (b) The cap and sites segments of the MH bundle. Helical wheels depict cross-sections (viewed in the top-down, HAMP to tip direction) of a four-helix knobs-in-holes (*a-d*) packing configuration. The descending helices (MH1, MH1') align with the ascending helices (MH2, MH2') in anti-parallel orientation. Each helix contains a series of seven-residue (heptad) repeats that comprise two helical turns and packing layers. Hydrophobic residues at *a* and *d* heptad positions promote the principal packing interactions between the bundle helices; edge residues at *e* and *g* heptad positions play ancillary roles in bundle geometry and stability. Adaptation site residues (stars) and adjacent D or E residues lie at solvent-exposed positions (*b, c, f*) that create extended acidic faces that modulate helix stability and packing in the MH bundle.

the kinase-OFF state and shifts them toward kinase-ON output (Parkinson et al. 2015).

Adaptational modifications adjust ligand sensitivity of the Tsr and Tar kinase control responses over more than a

hundred-fold range but produce only a few-fold shift in their ligand-binding affinities (Amin and Hazelbauer 2010a; Borkovich et al. 1992; Dunten and Koshland Jr. 1991; Iwama et al. 1997; Levit and Stock 2002; Lin et al. 1994). This mechanistic mystery has remained unsolved for decades. How can the receptor's mechanisms of ligand and sensory adaptation control of kinase activity operate so far out of equilibrium? To do so, ligand binding and sensory adaptation must modulate different structural properties of the signaling elements in receptor molecules (Bartelli and Hazelbauer 2016; Flack and Parkinson 2022; Hathcock et al. 2023; Le Moual et al. 1998).

The signaling architecture of MCP molecules can promote sensitive responses to small changes in chemoeffector concentration by coupling adjacent structural elements in dynamic opposition through special linkers (Figure 1a). Ligand-binding information from the periplasmic sensing domain and 4-helix transmembrane bundle modulates the stability and/or packing arrangement of a 4-helix HAMP bundle (Swain and Falke 2007; Zhou et al. 2009) through a five-residue control cable helix at the cytoplasmic side of the membrane (Ames et al. 2016; Kitanovic et al. 2011; Kitanovic et al. 2015) (Figure 1a). HAMP domains are versatile input-output relays in many microbial signaling proteins, particularly sensor Histidine kinases, Adenylyl cyclases, MCPs and some Phosphatases (reviewed in Parkinson 2010). The HAMP domain, through a 4-residue "phase stutter" connection, in turn influences the packing stability or geometry of the methylation helix (MH) bundle (Flack and Parkinson 2018, 2022; Zhou et al. 2009) (Figure 1a). Structural signals from the MH bundle travel to the hairpin bundle and tip through an intervening flexible bundle and glycine hinge (Alexander and Zhulin 2007; Coleman et al. 2005; Pedetta et al. 2017) that may couple their signaling structures in dynamic opposition as well (Swain et al. 2009).

The dynamic behaviors of the MH bundle have been extensively characterized with *in vitro* studies of the aspartate receptor Tar (Bartelli and Hazelbauer 2015; Bass and Falke 1998, 1999; Butler and Falke 1998; Danielson et al. 1997; Gordon et al. 2021; Greenswag et al. 2015; Kashefi and Thompson 2017; Koshy et al. 2013; Li et al. 2019; Malik et al. 2020; Samanta et al. 2015; Starrett and Falke 2005; Swain et al. 2009; Winston et al. 2005). Those studies have shown that the N-terminal MH1 helix is more dynamic than the C-terminal MH2 helix (Bartelli and Hazelbauer 2015) over nanosecond (Kashefi and Thompson 2017) to millisecond (Kashefi et al. 2019) timescales. The dynamic motions of both helices involve fluctuations in helicity and backbone motions, presumably reflecting transient excursions from stable helix-packing interactions in the

four-helix bundle (Bartelli and Hazelbauer 2015; Kashefi and Thompson 2017; Koshy et al. 2013; Samanta et al. 2015). Adaptational modifications influence the dynamic behaviors of both helices (Bartelli and Hazelbauer 2016; Malik et al. 2020), at least in part by altering the density of helix-destabilizing negative charges on solvent-exposed acidic faces of both helices (Starrett and Falke 2005) (Figure 1b). Overall, in Tar the MH1 helix is more dynamic than its MH2 partner and their packing interactions respond to adaptational modifications (Bartelli and Hazelbauer 2016; Kashefi et al. 2019; Koshy et al. 2013) and to structural changes induced by attractant ligands (Amin and Hazelbauer 2010b; Gordon et al. 2021) or by kinase-OFF receptor lesions (Kashefi and Thompson 2017).

In the present study we explored stimulus-triggered conformational and dynamic changes in the MH bundle of the serine receptor Tsr. We tracked these events in living cells through *in vivo* protein crosslinking methods that elucidate structural features of chemoreceptors (Flack and Parkinson 2022; Hughson and Hazelbauer 1996; Massazza et al. 2011; Watts et al. 2011) and their higher-order signaling complexes (Ames et al. 2002; Pedetta et al. 2014; Studdert and Parkinson 2004, 2005) under conditions that are difficult to replicate faithfully *in vitro*. Combined with *in vivo* FRET kinase assays, receptor crosslinking provides functional snapshots of helix packing configurations and motions for different signaling states in native receptor arrays (Flack and Parkinson 2022). With these approaches we have been able to follow the transmission of stimulus-induced signals through Tsr in unprecedented detail and have identified structural features that collectively regulate signal transmission and kinase output state.

2 | RESULTS

2.1 | Scanning for dynamic sites in the Tsr MH bundle

Helix packing in coiled-coils occurs mainly through hydrophobic interactions between residues at *a* and *d* positions in a repeating heptad pattern (Lupas and Gruber 2005) (Figure 1b). Residues at *e* and *g* heptad positions flank the hydrophobic core residues and can contribute to packing stability (Lupas and Gruber 2005), but are less critical to receptor function than are the hydrophobic packing residues at *a* and *d* heptad positions (Danielson et al. 1997; Flack and Parkinson 2018, 2022; Winston et al. 2005). To survey *in vivo* dynamic behaviors of the MH bundle helices we constructed mutations in Tsr expression plasmid pRR53 (Ames et al. 2002) that

introduced a cysteine replacement at an *e* or *g* heptad position. In all, we created 30 mutant plasmids, each encoding Tsr subunits with one cysteine residue (single-CYS). When expressed in a receptorless but otherwise wild-type host (UU2612), 24/30 of the mutant plasmids supported demonstrable serine chemotaxis in soft agar assays (Table S1) and all reporter proteins had intracellular amounts within two-fold of the wild-type level (Table S1), consistent with a native or near-native structure.

We expressed single-CYS receptors from the mutant plasmids in receptorless strain UU2610, which lacked the sensory adaptation enzymes CheR and CheB to simplify receptor immunoblot patterns (Flack and Parkinson 2022). Importantly, this host contained wild-type CheA and CheW to allow the receptors to assemble core signaling units (CSUs) (Figure S1) and arrays. We induced crosslinking by treating the cells with bismaleimidoethane (BMOE), a cell-permeable, bifunctional thiol-reactive crosslinking reagent with an 8 Å spacer (Flack and Parkinson 2022; Pinas et al. 2022; Scheinost and Gligoris 2018), using the same reaction conditions for all reporters (200 μM BMOE, 100", 30°C). Cell lysates were subjected to denaturing sodium dodecyl sulfate-polyacrylamide gel electrophoresis (SDS-PAGE) and Tsr subunits were detected and quantified by immunoblotting with a polyclonal rabbit antiserum raised against the highly conserved Tsr hairpin tip (Ames and Parkinson 1994; Studdert and Parkinson 2004). Figure S2a shows examples of the SDS-PAGE immunoblots.

We expected that dynamic motions of the MH bundle helices might bring the cysteine reporters in a Tsr dimer within BMOE crosslinking distance (5–10 Å) (Figure S1). It seemed less likely that BMOE would promote crosslinks between the receptor molecules in adjacent dimers within core signaling units because of the relatively long distances between the receptors in the trimer-of-dimers arrangement (Figure S1). In addition, the translational motions of receptors in CSUs are probably constrained by their periplasmic domains and by tight interactions between their hairpin tips and the CheA/CheW signaling proteins (Cassidy et al. 2023; Massazza et al. 2011) (Figure S1). We assume, therefore, that crosslinking in single-CYS receptors reflects dynamic motions within a homodimer rather than between the neighboring receptor molecules of core signaling units.

The MH1 and MH2 helices behaved comparably with respect to *e*-CYS reporters (Figure 2a). In cells not pre-exposed to serine, less than 10% of the reporter subunits formed dimeric crosslinking products, implying little dynamic motion of the MH bundle in the absence of a serine stimulus. However, in cells pre-treated with 10 mM serine, three MH1 reporters and three MH2 reporters crosslinked more substantially, ranging up to

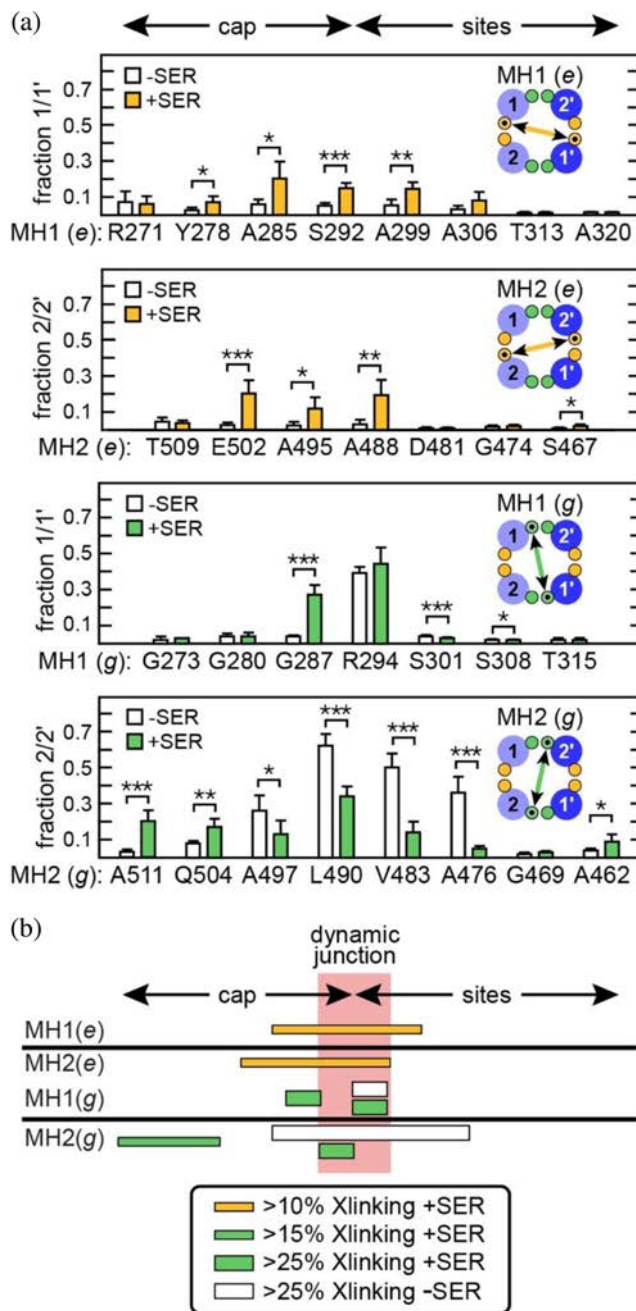


FIGURE 2 Evidence for a dynamic junction in the Tsr MH bundle. (a) BMOE crosslinking between Tsr subunits with a cysteine replacement at a bundle edge residue. The cartoon insets in each panel depict the subunit helices (light and dark blue), the positions of their *e* (orange) and *g* (green) edge residues and the crosslinked reporter sites (small black circles). Data are means and standard deviations from three or more biological replicates. Asterisks indicate reporter positions with significant \pm SER differences (white vs. colored bars) as determined by the following *p* values: <0.05 (*), <0.01 (**), or <0.001 (***). (b) Summary of the data in (a) that identifies a dynamic junction in the middle of the MH bundle.

20% yield of 1–1' or 2–2' products. Overall, *e*-residue sites at each end of the MH bundle exhibited little or no dynamic behavior either with or without serine

pretreatment, whereas *e* sites in the middle of the MH bundle showed serine-enhanced dynamics.

The MH1 g-CYS reporter sites at each end of the bundle exhibited low crosslinking with and without serine, much like the MH1 *e*-CYS reporters (Figure 2a). The MH2 g-CYS reporters were similarly quiescent at the sites end of the MH bundle, but more dynamic than their MH1 counterparts at the HAMP-proximal cap end of the MH bundle. Both MH1 and MH2 g-CYS reporters exhibited substantial crosslinking yields near the cap-sites junction. In MH1, the G287C reporter showed more than a five-fold crosslinking increase in the presence of serine and the adjacent R294C reporter exhibited over 40% crosslinking both in the absence and presence of serine (Figure 2a). Three MH2 g-CYS reporters spanning the cap-sites junction (L490C, V483C, A476C) showed 35%–60% crosslinking in the absence of serine, whereas pretreatment with serine *reduced* their crosslinking propensities by two-fold or more (Figure 2a).

These single-CYS crosslinking results indicate that serine stimuli differentially influence the dynamic behaviors of reporters in the MH1 and MH2 helices. The dynamics of both helices were most pronounced at the junction of the MH cap and sites segments, which we designate the dynamic junction of the MH bundle (Figure 2b). At the dynamic junction, serine enhanced crosslinking of the MH1 g-CYS reporter (R294C) and both MH1 (S292C) and MH2 (A288C) *e*-CYS reporters but suppressed crosslinking of L490C and other MH2 g-CYS reporters spanning the junction. Serine could conceivably reduce MH2 g-CYS crosslinking by altering the proximity of the reporter sites or by exacerbating their dynamic motions, either of which could reduce their dwell time in a crosslink-competent orientation. Overall, the elevated crosslinking behaviors induced by serine spread outward from the dynamic junction, mainly toward the HAMP-proximal cap end of the MH helices. The HAMP-distal sites end of the MH bundle exhibited no discernable dynamic behavior in single-CYS reporters (<10% crosslinking \pm SER). As we describe below, we interpret these results to show the dynamic junction plays a unique mechanistic role in signal transmission through the Tsr MH bundle and may account for the MH bundle structural dynamics previously documented with *in vitro* studies of the Tar receptor (Bartelli and Hazelbauer 2015, 2016; Bass and Falke 1998, 1999; Butler and Falke 1998; Danielson et al. 1997; Gordon et al. 2021; Greenswag et al. 2015; Kashefi and Thompson 2017; Koshy et al. 2013; Li et al. 2019; Malik et al. 2020; Samanta et al. 2015; Starrett and Falke 2005; Swain et al. 2009; Winston et al. 2005).

2.2 | Dynamic motions cause BMOE-dependent mobility shifts in Tsr monomers

During single-CYS crosslinking experiments, we noted that upon BMOE treatment many Tsr reporters produced a new SDS-PAGE band just above or below the monomer position (Figure S2a). Bandshifts occurred for both MH1 and MH2 single-CYS reporters and many of those evinced serine-enhanced effects (Figure S2a). Because the affected reporter sites spanned the dynamic junction and often exhibited serine-enhancement, we suggest that these effects arise from dynamic behaviors that provide BMOE access to the subunit reporter sites (summarized in Figure S2b).

Single amino acid replacements in MCP molecules can also produce modest shifts in subunit mobility in SDS-PAGE experiments, possibly by the same mechanism. The best examples are the effects of adaptational modifications: E residues at adaptation sites slow electrophoretic mobility, whereas methylated E or methylmimic Q residues speed mobility (Boyd and Simon 1980; Chelsky and Dahlquist 1980; DeFranco and Koshland Jr. 1980; Engstrom and Hazelbauer 1980). The mechanism behind these bandshifts is unclear but may reflect differences in the overall density of negatively charged SDS molecules that coat the receptor subunits (Sherris and Parkinson 1981). Thus, negative charges at key receptor positions might lead to slower gel migration by interfering with SDS binding. BMOE might produce a similar mobility shift by occasionally crosslinking an accessible cysteine in a Tsr subunit to glutathione or some other small, negatively-charged cytoplasmic component that bears a maleimide-reactive sulfhydryl group.

Cu²⁺-phenanthroline (CuPhen) treatment also produced monomer mobility shifts and dimer crosslinking products (Figure S2c). In 100-second reactions CuPhen and BMOE produced similar extents of dimeric crosslinking products, but the shifted monomer products accumulated more slowly under CuPhen conditions, implying that the shift effect involves an intrinsically slower reaction than does subunit–subunit crosslinking (Figure S2c). The band-shifted CuPhen species reverted to monomers upon treating the samples with a reducing agent, but reducing treatment had little effect on the band-shifted monomers produced by BMOE (Figure S2c). These results are consistent with the possibility that disulfide (CuPhen) or maleimide (BMOE) linkage to a thiol-bearing compound like glutathione produces the band-shifted species. We conclude that the monomer bandshift effect provides a fortuitous and reproducible means of assessing receptor dynamic behavior independently

of subunit-subunit crosslinking. Both readouts identify similar dynamic regions in the MH1 and MH2 helices that span the dynamic junction (Figure S2b).

2.3 | Signaling behaviors of single-CYS Tsr reporters

We used an *in vivo* assay based on Förster resonance energy transfer (FRET) (Lai and Parkinson 2014; Sourjik et al. 2007; Sourjik and Berg 2002) to assess the CheA-control signaling behaviors of the Tsr single-CYS receptors. This assay measures interaction between fluorophore-tagged CheY (yellow fluorescent protein, YFP) and its phosphatase partner CheZ (cyan fluorescent protein, CFP). CheA-mediated phosphorylation of CheY-YFP promotes binding with CheZ-CFP, producing a FRET signal that reflects cellular phospho-CheY levels and, in turn, the receptor-controlled kinase activity of CheA. Serine dose-response experiments were conducted in host strain UU2567 (Lai and Parkinson 2014), a close relative of the UU2610 strain used for the single-CYS crosslinking surveys. In that strain, which lacks the sensory adaptation enzymes, Tsr in the wild-type (QE_{QEE}) modification state inhibits 50% of CheA activity at 15–20 μ M serine, its $K_{1/2}$ response value (Ames et al. 2016; Flack and Parkinson 2018, 2022; Gao et al. 2019; Han and Parkinson 2014; Kitanovic et al. 2015; Lai et al. 2017; Lai and Parkinson 2014).

Tsr *e*-CYS reporters were generally OFF-shifted in FRET assays, with only one receptor showing a serine response threshold above the wild-type (Figure S2d). In contrast, *g*-CYS receptors were generally ON-shifted in FRET assays, with all but two above the wild-type $K_{1/2}$ (Figure S2d). These results show that cysteine replacements at *g*-position residues shift Tsr output toward the ON state and replacements at *e*-position residues shift output toward the OFF state. These mutant behaviors imply that the native *g* residues of the Tsr MH bundle play important roles in promoting kinase-OFF output, whereas *e* residues are important for kinase-ON output.

2.4 | Crosslinking surveys of CYS-pair receptors in the Tsr MH bundle

To investigate how serine-induced conformational signals propagate through the Tsr dynamic junction, we followed *in vivo* BMOE-promoted crosslinking between pairs of cysteine replacements at heptad edge-residue (*e*, *g*) positions. Our working model posits that serine stimuli induce axial helix rotations that shift the MH bundle

from a conventional “knobs-in-holes” *a-d* packing arrangement in the ON state to a complementary *x-da* OFF-state arrangement in which the edge residues at *g* positions rotate toward the bundle core and edge residues at *e* positions rotate away from the packing core (Figure 3a) (Flack and Parkinson 2022). We constructed Tsr reporters bearing adjacent pairs of *g*-CYS sites (designated *g/g* or *g/g*-CYS receptors; Table S1 and Figure S3b). Note that adjacent *g*-position residues in the MH1 and MH2' helices have a staggered arrangement (Figure S3). Such *g/g* reporter sites would be expected to move closer and crosslink more readily in the presence of serine, according to our working model (Figure 3a).

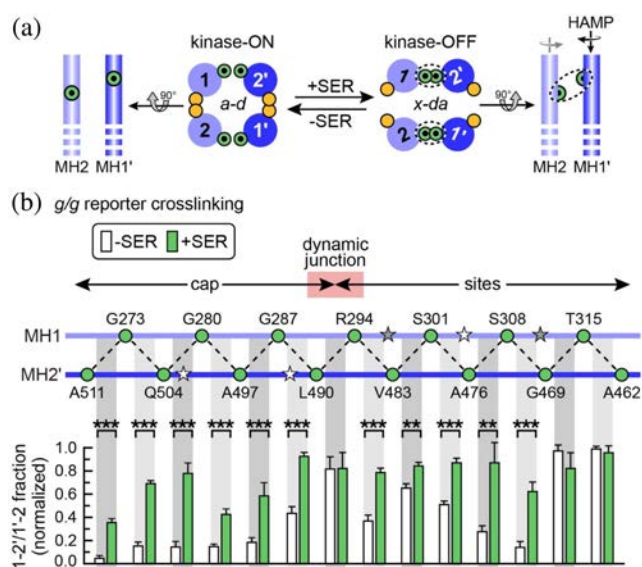


FIGURE 3 BMOE crosslinking scan of *g/g* reporter pairs in the Tsr MH bundle. (a) Working model of MH bundle packing and signaling configurations. The cartoons depict the subunit helices (light and dark blue), the positions of their *e* (orange) and *g* (green) edge residues and the cysteine reporter sites (small black circles). Serine-induced axial rotation is predicted to enhance crosslinking of *g/g* reporter pairs by shifting the MH bundle from *a-d* (ON) to *x-da* (OFF) packing (Flack and Parkinson 2022). (b) *g/g* cysteine pairs surveyed. Cysteine replacements were created at each of the indicated *g*-position residues, then combined to make Tsr subunits bearing adjacent *g/g* pairs (dashed lines). Stars represent wild-type Tsr adaptation site residues (white, E; gray, Q) that were not manipulated in these experiments. To simplify the data presentation, sites are shown evenly spaced between the helices, but darker gray shading indicates the longer distance *g/g* pairs. See Figure S4 for a more accurate structural view. Crosslinking data are means and standard deviations for doubly-crosslinked (1-2'/1'-2) products from three or more biological replicates normalized to the highest value (T315C/A462C-SER). Raw data values for these experiments are given in Table S2. Asterisks indicate reporter positions with significant \pm SER differences as determined by the following *p* values: <0.01 (**), or <0.001 (***).

We tested *g/g* crosslinking behaviors with the same BMOE reaction conditions used for the single-CYS receptors (see Figure S4a,b for representative SDS-PAGE band patterns and how we identified and quantified the various crosslinked products. Note that there are no band-shifted monomers in the *g/g* lanes, confirming that the dimeric crosslinking reactions are much faster). Under these conditions serine produced highly significant increases in the 1-2'/1'-2 doubly crosslinked BMOE product for all six MH cap reporter pairs and for five reporter pairs in the MH sites region (Figure 3a,b). Three reporter pairs (R294C/L490C at the dynamic junction and T315C/G469C and T315C/A462C at the HAMP-distal end of the MH sites segment) exhibited comparably high crosslinking signals in the absence, as well as presence, of serine (Figure 3b). Crosslinking timecourses of these highly reactive *g/g* reporter pairs at a 10-fold lower BMOE concentration showed that their doubly crosslinked product formed more rapidly in serine-exposed cells than it did in buffer-treated controls (Figure S4c). Thus, *g/g* reporters throughout the MH bundle underwent demonstrable signaling-related structural changes consistent with serine-induced *a-d* to *x-da* packing transitions at the reporter sites.

A key prediction of this signaling model not previously tested is that adjacent *e*-position cysteines in MH1 and MH2, which also have a staggered arrangement (Figure S3), should crosslink more readily in the absence of serine because *e/e* reporter sites lie closer in the *a-d* bundle configuration than in the serine-promoted *x-da* packing arrangement (Figure 4a). Accordingly, we surveyed a corresponding set of *e/e* reporter pairs across the Tsr MH bundle (Figure 4). These should (Figure 4a) and did (Figure S5) form monomer-sized crosslinking products. Initial experiments done with BMOE reaction conditions optimal for *g/g* reporters produced high levels of *e/e* crosslinking in both the absence and presence of serine. Based on reaction timecourses at lower BMOE concentrations (Figure S5a,b), we chose a 10-fold lower BMOE concentration (20 μ M), a 10-fold shorter reaction time (10''), and a lower acrylamide concentration (8%) to better resolve the *e/e* crosslinking products and serine-related effects. Some *e/e*-crosslinked subunits migrated slower in SDS-PAGE immunoblots than did uncrosslinked Tsr subunits; others migrated faster, depending on the positions of the reporter sites along the MH bundle (Figure S5c).

The *e/e* reporter pairs showed substantial differences in the extent of crosslinking through the MH bundle (Figure 4b), likely reflecting sequence-specific contributions to bundle stability by the residues flanking the reporter sites in the surveyed heptads. Six reporter pairs

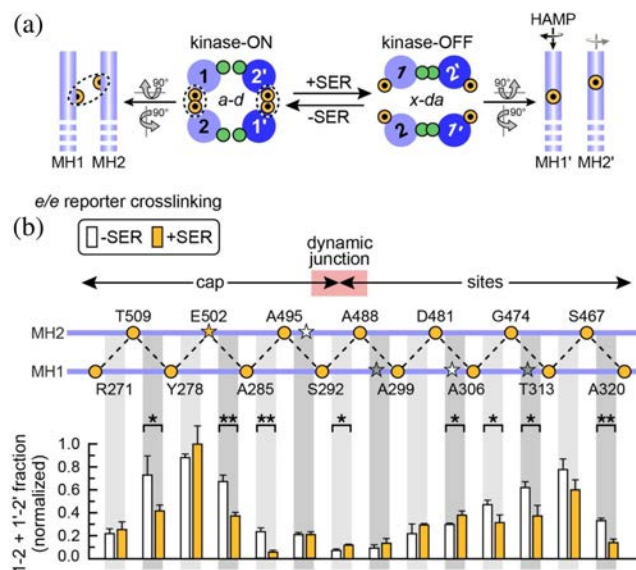


FIGURE 4 BMOE crosslinking scan of *e/e* reporter pairs in the Tsr MH bundle. (a) Working model of MH bundle packing and signaling configurations. The cartoons depict the subunit helices (light and dark blue), the positions of their *e* (orange) and *g* (green) edge residues and the crosslinked reporter sites (small black circles). Serine-induced axial rotation of the MH1 helices is predicted to inhibit crosslinking of *e/e* reporter pairs by shifting MH bundle packing toward an *x-da* (kinase-OFF) configuration, whereas adjacent *e/e* reporter sites should be closer and more readily crosslinked in an *a-d* (kinase-ON) packing arrangement. (b) *e/e* cysteine pairs surveyed. Cysteine replacements were created at each of the indicated *e*-position residues, then combined to make Tsr subunits bearing adjacent *e/e* pairs (dashed lines). Stars represent wild-type Tsr adaptation site residues (white, E; gray, Q) that were not manipulated in these experiments. To simplify the data presentation, sites are shown evenly spaced between the helices, but darker gray shading indicates the longer distance *e/e* pairs. See Figure S4 for a more accurate structural view. Crosslinking data are means and standard deviations for intra-subunit crosslinking products (1-2 and 1'-2') from three or more biological replicates normalized to the highest value (Y278C/E502C + SER). Raw data values from these experiments are given in Table S2. Asterisks indicate reporter positions with significant \pm SER differences as determined by the following *p* values: <0.05 (*) or <0.01 (**).

(three in the cap and three in the sites region) crosslinked significantly more in the absence than in the presence of serine (Figure 4b), confirming that the serine-induced bundle arrangement slows crosslinking between CYS reporter sites at those MH1/MH2 *e*-heptad positions. Reaction timecourses might reveal significant serine-dependent crosslinking differences for other *e/e* CYS pairs, but we did not pursue that issue in the present study.

2.5 | BMOE crosslinking shifts Tsr *g/g* receptors toward kinase-OFF output and *e/e* receptors toward kinase-ON output

In FRET kinase assays, the behaviors of CYS-pair reporters were like, but in some cases more extreme than, their single-CYS components (Table S1). Six *g/g* reporters exhibited an elevated $K_{1/2}$ value, consistent with ON-shifted signaling properties. Eight other *g/g* receptors failed to respond to even 10 mM serine, but their FRET signal dropped substantially when the cells were challenged with 3 mM potassium cyanide (KCN). KCN treatment collapses cellular ATP levels, the phosphodonor for CheA autophosphorylation, and consequently prevents CheA-mediated phosphorylation of CheY (Lai and Parkinson 2014) (Figure S6a). By contrast, eight *e/e* reporters were kinase-OFF and five others had OFF-shifted serine responses with $K_{1/2}$ values below the wild-type (Table S1). As with the single-CYS reporters, these mutant output behaviors imply that the native Tsr *g* and *e* residues of the MH bundle play important roles in promoting kinase-OFF and kinase-ON CheA outputs, respectively.

The MH1 helix-rotation model predicts that because BMOE crosslinks are irreversible, crosslinking should trap the helices of Tsr *g/g* receptors in the rotated state and reduce or eliminate their kinase activity. This effect proved true for 4/5 MH cap *g/g* receptors in our earlier study (Flack and Parkinson 2022). That trend prevailed in 8/9 additional MH bundle *g/g* reporters, which were driven to lower $K_{1/2}$ or fully kinase-OFF behavior by BMOE exposure in the FRET assay (Figure S6). The one exception was the S308C/G469C reporter near the HAMP-distal end of the MH bundle. This receptor remained locked in kinase-ON output after challenge with a combination of serine plus BMOE (Figure S6a), similar to one serine non-responsive *g/g* reporter in the cap (Flack and Parkinson 2022).

We examined five *e/e* reporters for BMOE signaling effects in the FRET assay; all five showed behaviors consistent with the prediction that *e/e* crosslinks would shift output toward the kinase-ON state (Figure S7). BMOE abolished serine responses of the Y278C/E502C receptor and locked it in kinase-ON output (Figure S7a). Remarkably, two kinase-OFF reporters (R271C/T509C, S292C/A495C) became kinase-active following BMOE exposure and readily responded to small serine stimuli ($K_{1/2}$ values below 1 μ M) (Figure S7b). Two other kinase-active, serine-responsive receptors (Y278C/T509C, A306C/G474C) retained kinase activity after BMOE treatment but became much less sensitive to serine (>100-fold higher $K_{1/2}$ values), again consistent with a crosslinking-induced shift toward the ON output state (Figure S7c).

These results demonstrate a relationship between the extent of BMOE crosslinking and the degree to which BMOE treatment shifted *g/g* receptors toward kinase-OFF output and *e/e* receptors toward kinase-ON output. The Tsr molecules in our crosslinking and FRET experiments assemble arrays of cooperatively networked signaling teams, so not all cell receptors would necessarily need to be crosslinked to lock array output in an ON or OFF state. Conversely, owing to variable sizes and connectivities of receptor signaling teams within arrays, even extensively crosslinked arrays could retain some kinase activity after BMOE treatment.

2.6 | Crosslinking and kinase-control behaviors of CYS-pair receptors

A comparison of the crosslinking and kinase-control behaviors of CYS-pair reporters shows that these two signaling readouts differ in stimulus sensitivity (Figure 5). Seven *e/e* reporters spanning the dynamic junction were locked-OFF in FRET assays, indicating that their hairpin tip produced no detectable CheA activity. Yet reporters at each end of the dynamic junction exhibited significant serine-dependent crosslinking effects: serine inhibited crosslinking of the E502C/A285C and A285C/A495C cap reporters and enhanced crosslinking of the D481C/A306C sites reporter (Figure 4). Evidently, the locked-OFF conformation at the hairpin tip does not reflect the reporter conformation in the MH bundle, which is still responsive to a serine stimulus. The disparity between crosslinking and FRET readouts was even more striking for the *g/g* reporters: eight exhibited serine non-responsive, locked-ON kinase activity in FRET assays, yet serine treatment substantially increased crosslinking for six of them, from Q504C/G280C in the cap to A476C/S308C in the sites (Figures 3 and 5). These findings demonstrate that for some reporter pairs, in vivo crosslinking assays can reveal serine-induced responses that the FRET kinase assay cannot.

Our crosslinking assays effectively produce short-exposure snapshots of MH bundle packing arrangements. These conformational readouts detect helix-packing responses to attractant stimuli within individual receptor dimers and do not depend on the higher-order interactions of receptors in core signaling units or arrays (Amin and Hazelbauer 2010b; Flack and Parkinson 2022). In a two-conformation (*a-d* versus *x-da*) model of Tsr MH bundle output states the extent of *e/e* crosslinking in the presence of serine should reflect a receptor's ON conformational bias at the reporter sites. Conversely, the extent of *g/g* crosslinking in the absence of serine should reflect a receptor's OFF conformational bias at the reporter sites.

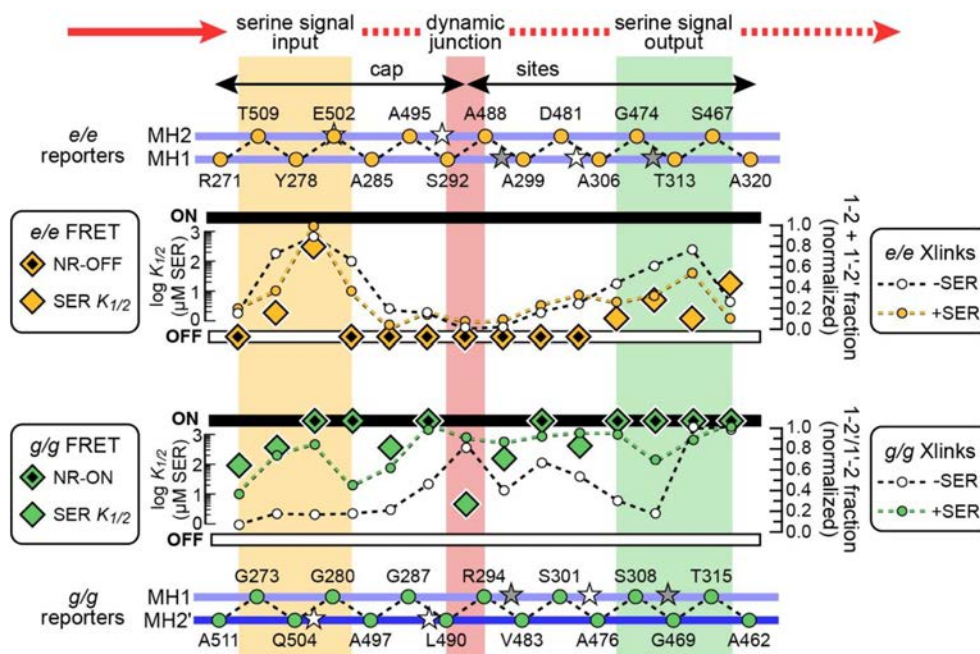


FIGURE 5 Comparison of crosslinking and kinase-control behavioral readouts for CYS-pair reporters. These data illustrate behavioral differences between the serine signal input and output segments of the MH bundle. The helix cartoons at top and bottom depict the subunit helices (light and dark blue) and the positions of their *e* (orange) or *g* (green) residues. Stars indicate the approximate positions of the wild-type E (white) and Q (gray) adaptation sites that were not manipulated in these experiments (top panel) *e/e* CYS-pair receptors. The data show FRET values for *uncrosslinked* receptors from Table S1 (UU2567 host) and the normalized crosslinking values from Figure 4b (UU2610 host; CheRB⁻). NR-OFF receptors exhibited no response to serine stimuli up to 10 mM and no FRET change in response to 3 mM KCN, indicative of no CheA activity (Lai and Parkinson 2014). (bottom panel) *g/g* CYS-pair receptors. The data show FRET values for *uncrosslinked* receptors from Table S1 (UU2567 host; CheRB⁻) and the normalized crosslinking values from Figure 3b (UU2610 host; CheRB⁻). NR-ON receptors exhibited kinase activity upon KCN challenge (Lai and Parkinson 2014), but failed to inhibit that activity when challenged with 10 mM serine.

Although the *e/e* and *g/g* data were obtained with different reaction conditions, their normalized values permit useful comparisons between them.

The conformational bias estimates revealed three MH bundle regions with distinctive signaling behaviors: The HAMP-proximal (serine signal input) end of the bundle had ON-biased conformation; the HAMP-distal (serine signal output) end of the bundle had moderate OFF-biased conformation. The dynamic junction showed a strongly OFF conformational bias: high *g/g* crosslinking levels in the presence and absence of serine and very little *e/e* crosslinking under either condition. The high OFF bias at the dynamic junction progressively diminished through the sites segment until again peaking at the signal output end of the MH bundle (Figure 5).

2.7 | AlphaFold insights into MH bundle signaling structures

We generated atomic structures of the full-length Tsr dimer with AlphaFold 2 (Jumper et al. 2021) and AlphaFold 3 (Abramson et al. 2024) and analyzed their MH

bundle packing arrangements with SamCC Turbo, which computes Crick angles (sidechain orientations) in 4-helix coiled-coil bundles (Szczepaniak et al. 2021). Both Tsr structures showed MH2 Crick angle deviations characteristic of *x-da* packing over residues 486–494 spanning the dynamic junction (Figure 6a). The corresponding segment of the MH1 helices showed a similar but less pronounced rotation trend (Figure 6a). Rotation of the MH2 helix into an *x-da* packing orientation at the dynamic junction coincided with a pronounced bulge and kink (Figure 6b), similar to a feature noted in the crystal structure of Tm14, a soluble MCP of *Thermotoga maritima* (Pollard et al. 2009). The Crick angle deviations indicate the input and output ends of the MH bundle had *a-d* packing configurations, whereas the dynamic junction showed *x-da* packing (Figure 6c,d). These structural features suggest the dynamic junction adopts an *x-da* packing arrangement in the absence of a serine stimulus and that rotation of the MH2 helix is the principal driving force for that configuration, which would explain the very high crosslinking of MH2 *g*-CYS reporters that span the dynamic junction (Figure 2). These findings provide a structural context for the unique crosslinking behaviors

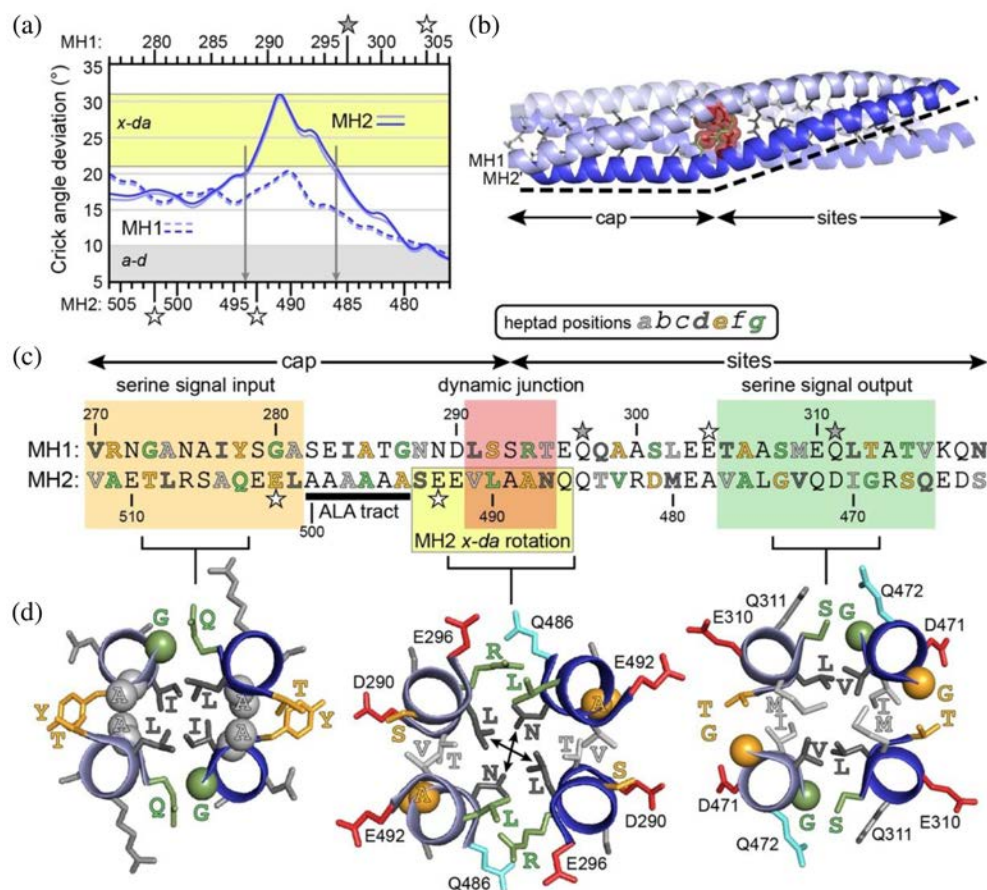


FIGURE 6 Signaling-related structural features of the MH bundle and dynamic junction. (a) Crick angle deviations (axial rotations) of MH1 and MH2 residues from a SamCC Turbo analysis (Dunin-Horkawicz and Lupas 2010b) of atomic coordinates for a full-length Tsr dimer generated by AlphaFold 3 (Abramson et al. 2024). Typical angles for *a-d* packed residues are $\pm 10^\circ$; *x-da* packed residues average 26° (Dunin-Horkawicz and Lupas 2010b). (b) Structure of the MH bundle in an AlphaFold 3 model of the Tsr dimer. Side-chains of residues at *a* (light gray) and *d* (dark gray) positions are shown as sticks. Semi-transparent spheres represent side-chain atoms of the dynamic junction *d*-heptad residues L291 and N487. Green sticks show side-chains of dynamic junction *g*-heptad residues R294 and L490. The dashed line traces a pronounced bulge and kink at the dynamic junction. (c) Primary structure and key regions of the Tsr MH bundle. (d) One-heptad slab views of packing configurations in the AlphaFold 3 Tsr model. Key residues are labeled and color-coded to the sequence in (c); negatively charged residues are shown in red. Glycine residues are shown as a sphere; C α and C β atoms of alanine sidechains otherwise difficult to discern are also shown as spheres. Arrows in the dynamic junction structure indicate *x* positions in the *x-da* packing configuration. Methylation site Q311 influences MH bundle conformation and dynamics; the other cyan-colored glutamine residues may also.

of the dynamic junction and suggest a mechanism for signal propagation through the MH bundle, as discussed below.

3 | DISCUSSION

3.1 | Signaling-related conformations in the Tsr MH bundle

Three lines of evidence indicate that *x-da*-like packing arrangements of the Tsr MH bundle produce kinase-OFF output: (i) Residues at adjacent MH1 and MH2 *g*-heptad positions lie closer in the *x-da* arrangement than they do

in the *a-d* configuration (Figure 3a) and OFF-shifting serine stimuli enhanced BMOE crosslinking of *g/g* reporter pairs (Figure 3b). (ii) Most *g*-position cysteine replacements shifted Tsr output toward the ON state (Figures S2d and 5 and Table S1), suggesting that destabilization of the packing arrangement promoted by native *g*-position residues reduces kinase-OFF output. Conceivably, the electron-rich sulfur groups in the cysteine reporters repulse one another to shift packing toward the *a-d* arrangement. (iii) BMOE crosslinking of *g/g* reporter pairs shifted their output back toward the kinase-OFF state (Figure S6b-d).

Analogous evidence indicates that *a-d*-like packing configurations of the Tsr bundle produce kinase-ON

output: (i) Residues at adjacent MH1 and MH2 *e*-heptad positions lie closer in the *a-d* arrangement than they do in the *x-da* configuration (Figure 4a) and OFF-shifting serine stimuli slowed BMOE crosslinking of *e/e* reporter pairs (Figure 4b). (ii) Most *e*-position cysteine replacements shifted Tsr output toward the OFF state (Figures S2d and 5 and Table S1), suggesting that destabilization of the packing arrangement promoted by native *e*-position residues reduces kinase-ON output. Repulsion between cysteines at the *e* positions should shift packing toward the *x-da* arrangement. (iii) BMOE crosslinking of *e/e* reporter pairs shifted their output back toward the kinase-ON state (Figure S7).

3.2 | A three-state signaling model for the Tsr MH bundle

The crosslinking behaviors of CYS-pair receptors indicate that signaling through the Tsr MH bundle can be

understood in terms of a three-state structural model involving kinase-ON (*a-d*-like) and kinase-OFF (*x-da*-like) helix-packing arrangements linked through unstable or unstructured intermediates (Figure 7). The HAMP domain, which provides conformational input to the MH bundle, probably has analogous signaling modes (Dunin-Horkawicz and Lupas 2010a; Ferris et al. 2011; Hulko et al. 2006; Parkinson 2010), but we do not consider those here. A four-residue phase stutter couples the HAMP AS2 helices to the MH1 helices in opposed packing arrangements, such that an *x-da* packed HAMP bundle should favor *a-d* packing of the MH cap, whereas an *a-d* HAMP bundle should favor *x-da* packing of the MH cap (Ferris et al. 2011, 2014; Flack and Parkinson 2018, 2022) (Figure 7). Thus, interconversion of the *a-d* and *x-da* configurations in the signal input and output ends of the MH bundle requires HAMP-promoted axial rotation of the MH1 helices and counter-rotation of the MH2 helices to optimize stability at their packing interfaces (Ferris et al. 2014; Flack and Parkinson 2022).

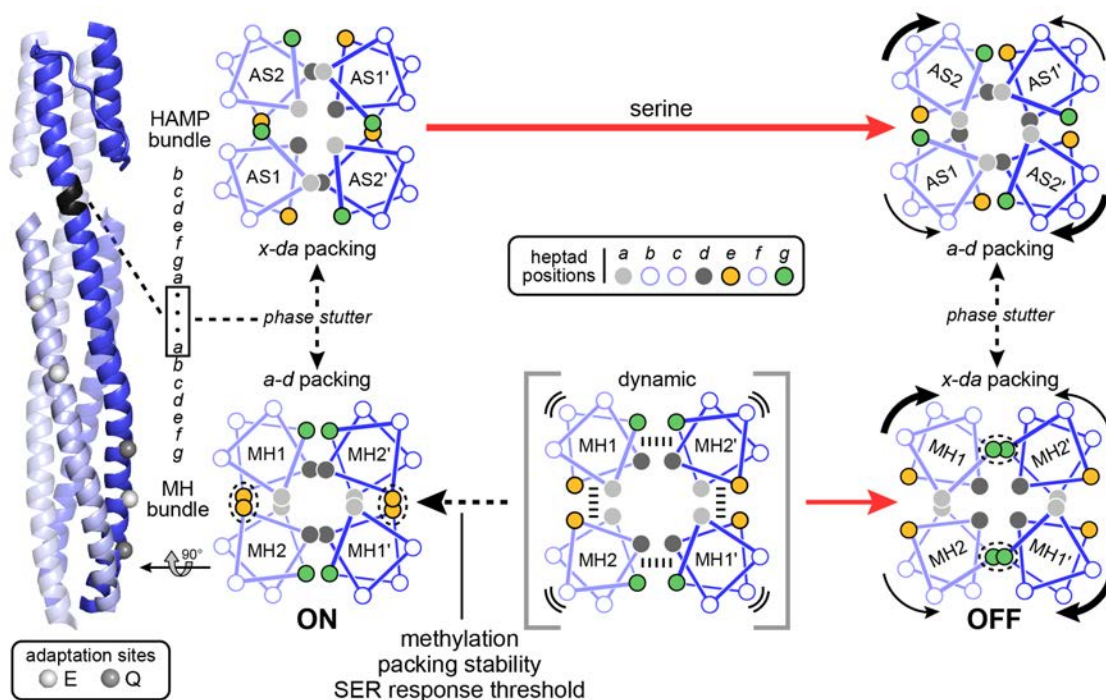


FIGURE 7 Three state model of MH bundle signaling in Tsr. The ribbon diagram at left shows subunits of the HAMP and MH bundles of a Tsr dimer extracted from a model of the core signaling unit (Cassidy et al. 2023), with helices at the rear dimmed and colors keyed to the helical wheels to the right. Spheres depict the alpha carbons of E (white) and Q (gray) adaptation site residues. The 4-residue phase stutter (black) joins the AS2 and MH1 helices $\sim 26^\circ$ out of register. For simplicity, the first three residues of the stutter helix lack a heptad designation (\bullet); the last stutter residue (V267 in Tsr) occupies an *e*-heptad position in the AS2 register, but an *a*-heptad position in the MH1 register. Helical wheel diagrams depict top-down cross-section views through the bundles. Due to the phase stutter, an *a-d* packed HAMP bundle favors an *x-da* packed MH bundle, whereas an *a-d* packed MH bundle favors *x-da* packing of HAMP. Black curved arrows indicate the directions of helix rotations; thick curved arrows indicate the serine-imposed helix rotations through the phase stutter connections. Dashed lines between helices in the dynamic intermediate state represent the principal helix-helix interactions that modulate MH bundle packing stability. In the presence of serine (SER) the MH bundle is in rapid equilibrium between *x-da* packing and dynamic states. The adaptational modification state of Tsr (“methylation”) spans a range from fully unmodified (5E) to fully modified (methylated E or methylmimic Q) residues per subunit. Higher methylation states shift the receptor toward more stable *a-d* packing and higher serine response thresholds.

Conserved, but often atypical, *a* and *d* packing residues (Figure S8) could moderate helix-pairing interactions from one heptad to another throughout the MH bundle. Conserved acidic residues on solvent-exposed faces of the MH1 and MH2 helices (Figures 1b and S8) also contribute to MH bundle dynamics. These acidic faces create an extended negatively charged surface that could contribute to bundle dynamics by reducing helix stability (Starrett and Falke 2005). Three of the MH1 acidic-face residues are sensory adaptation sites, where methylation or a neutral sidechain replacement would reduce overall negative charge on the acidic face and thereby enhance MH1 helicity and packing interactions. Indeed, *in vitro* studies of full-length Tar dimers in nanodiscs and soluble Tar signaling fragments found that MH1 was more dynamic and less helical in the (EEEE) state than in the (QQQQ) modification state (Bartelli and Hazelbauer 2016; Kashefi and Thompson 2017). The MH2 helix also has solvent-exposed acidic faces flanking the dynamic junction that might modulate helix stability in a similar fashion (Starrett and Falke 2005) (Figures 1b and S8). Two of the residues in the acidic face that spans the MH2 alanine tract (Flack and Parkinson 2018) are sites of adaptational modifications in Tsr (Han and Parkinson 2014; Rice and Dahlquist 1991).

Our three-state signaling model proposes that the *a-d* and *x-da* packing states are in equilibrium with more dynamic bundle configurations, with the transition rate toward *a-d* packing controlled by adaptational modifications and toward *x-da* packing by chemoeffector stimuli (Figure 7). Although adaptational modifications might impact the helix stability needed for packing interactions common to both bundle arrangements, there is as yet little evidence bearing directly on this issue. However, serine-induced helix rotations can specifically alter the relative strengths of intra- and inter-subunit helix interactions, thereby promoting a bundle-packing geometry (*x-da*) that, with the notable exception of the dynamic junction, is seldom accessed through dynamic motions alone at any modification state.

3.3 | Signaling role of the dynamic junction

Tar receptors with single-CYS reporters form crosslinks *in vitro* over long-duration CuPhen treatments at essentially any MH bundle residue position (Danielson et al. 1997; Winston et al. 2005). By contrast, *in vivo* BMOE crosslinking assays with Tsr reporters capture short-exposure snapshots of the predominant dynamic motions in the MH bundle helices, more clearly reflecting the relative stabilities of their various pairing

interactions. Single-CYS reporters and *g/g* CYS-pair reporters crosslinked most readily at a “dynamic junction” between the MH cap and sites segments (Figures 2 and 5). These behaviors are consistent with the MH1 helix dynamics documented in Tar (Bartelli and Hazelbauer 2015, 2016; Kashefi and Thompson 2017). In addition, Bartelli and Hazelbauer noted that the highly mobile component at one of their Tar spin-label positions was three to four-fold greater than at either flanking reporter site (Bartelli and Hazelbauer 2015). That highly dynamic reporter site (Tar-284/Tsr-286) abuts the Tsr dynamic junction and rotated MH2 segment (Figure 6c), implying that Tar also has a dynamic junction at its cap-sites border.

Several lines of evidence indicate that the Tsr dynamic junction favors an *x-da* packing arrangement in the absence of a serine stimulus. First, the unliganded AlphaFold-generated Tsr structures exhibited MH2 rotation and *x-da* packing at the dynamic junction (Figure 6). The conserved MH2 alanine tract residues (Figures 6 and S8) might facilitate MH2 Crick angle transitions from *a-d* packing in the MH cap to *x-da* packing at the dynamic junction. The conserved LLF motif cap residues (Figure S8) might distort the geometry of *a-d* packing layers in the cap (Flack and Parkinson 2018) to facilitate the transition to *x-da* orientation through the alanine tract. Second, single-CYS and CYS-pair reporters at the dynamic junction *g*-position residues (R294, L490) crosslinked extensively with or without serine (Figures 2 and 3), whereas the corresponding *e*-site reporters (S292, A488) exhibited very little crosslinking in the absence of serine (Figures 2 and 4). Moreover, the R294 and L490 side-chains are distinctly different from those at *g* positions elsewhere in the MH bundle (Figure S8). Third, most residues at the dynamic junction are highly conserved and four of them in combination (R294, T295, L490, V491) are unique to Tsr, Tar, and other 36H class MCPs (Figure S8) (Alexander and Zhulin 2007). Another highly conserved dynamic junction residue, N487 (Figures 6d and S8), corresponds to the site of the bulge and kink in the Tm14 structure (Pollard et al. 2009).

3.4 | Signal transmission through the Tsr MH bundle

At the wild-type (QEQUEE) modification state used for all crosslinking assays in the present study, the Tsr dynamic junction seems to be uniquely poised to facilitate serine-induced transitions to OFF-state (*x-da*) packing interactions throughout the MH bundle (Figure 8). In the absence of a serine stimulus, the upstream signal input cap had a strong *a-d* packing bias, whereas the

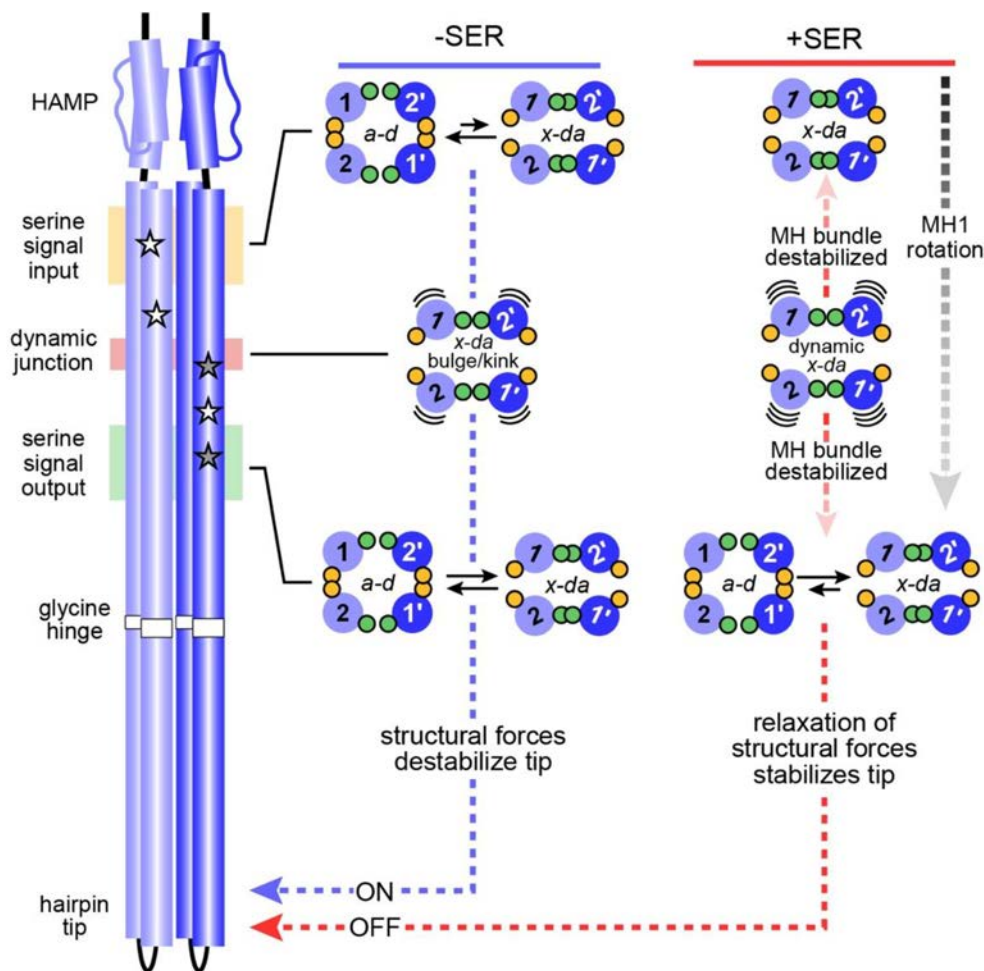


FIGURE 8 Signal transmission model for the Tsr MH bundle. Cylinders represent alpha-helical segments of Tsr subunits (light and dark blue) of the cytoplasmic domain drawn approximately to scale. Stars indicate adaptational modification site residues, E (white) and Q (gray). Proposed helix-packing configurations in the absence (–SER) and presence (+SER) of a serine stimulus are shown for the signal input, dynamic junction, and signal output regions of the MH bundle. Light and dark blue circles depict simplified top-down cross-section views of the alpha helices with only *e* (orange) and *g* (green) heptad positions shown. The relative lengths of the horizontal black arrows reflect the equilibrium bias between *a-d* and *x-da* packing configurations. Curved black lines represent increased dynamic behavior of the helices. MH1 and MH2 residues of the dynamic junction promote MH2 rotation and *x-da* packing at the dynamic junction, which spreads to the input and output segments upon serine-promoted rotation of the MH1 helix. Methylation of the MH1 and MH2 adaptation sites (not shown in this diagram) produces sensory adaptation by enhancing *a-d* packing of the MH bundle (see Figure 7). Refer to the text for further explanation and discussion of the model.

downstream signal output end of the MH bundle had more balanced *a-d* and *x-da* packing modes in evidently rapid equilibrium (Figure 5). The unstable character of the *x-da* configuration at the intervening dynamic junction extended a bit in both directions through dynamic motions of the MH2 and, to a lesser extent, the MH1 helices (Figures 2 and S2b).

Serine stimuli produced a dramatic shift toward *x-da* packing throughout the bundle. The cap adopted an *x-da* configuration with little evidence of *a-d* packing; the bundle output end became *x-da* biased, although it still underwent frequent transitions to *a-d* packing (Figure 5). These changes appear to stem from HAMP-induced axial

rotations of the MH1 helices, which probably reinforce MH2 rotation at the dynamic junction and propagate that MH2 *x-da* orientation to the input and output regions of the bundle (Figure 8). Importantly, the expanded scope of *x-da* packing promoted by serine does not stabilize overall bundle structure, but rather makes it more dynamic, probably due to the sidechain characters of the MH bundle packing and edge residues (Figures 2, 5, and S8). Equally important, *x-da* packing competes with *a-d* packing, thereby shifting overall bundle output toward the kinase-OFF state (Figures 3 and 4). In the presence of serine, packing evidently becomes less stable at the dynamic junction (Figure 8), perhaps reflecting the

overall rise in bundle dynamic motions (Figures 2 and S2). This change would account for the enhancing effects of serine on crosslinking of single-CYS reporters at the dynamic junction and its flanking regions (Figure 2). We suggest that overall enhanced dynamic behavior could also account for the serine-induced *reduction* in crosslinking of single-CYS MH2-g reporters across the dynamic junction to more closely match the behavior of their MH1-g counterparts (Figures 2 and S2b).

3.5 | Signal transmission from the MH bundle to the Tsr hairpin tip

This study further substantiates the dynamic-bundle model of HAMP domain input–output signaling in chemoreceptors, which proposed that attractant stimuli destabilize MH bundle structure to transmit kinase-OFF control signals to the receptor tip (Parkinson 2010; Zhou et al. 2009). Our crosslinking results indicate that to reach an effective OFF output state, the MH bundle shifts toward more dynamic *x-da*-packing configurations. The “yin-yang” signaling hypothesis (Swain et al. 2009) proposed that the MH bundle and hairpin tip are also coupled in structural opposition, in which case an unstable MH bundle should promote a more static, kinase-OFF hairpin tip. Consistent with this idea, charge reversals and small (G) or large (W) replacements at a salt-bridge residue pair known to stabilize the hairpin tip of Tsr shifted output toward the ON state (Gao et al. 2019), suggesting that a destabilized tip has kinase-ON activity.

The conformational and dynamic changes detected in our crosslinking assays occur within individual receptor molecules, and because some CYS-pair receptors yielded crosslinking fractions above 80% in array-competent cells (Table S2), we conclude that all receptors in core signaling units have comparable structures at the level of the MH bundle (Figure S1). However, the receptor dimers converge through the flexible bundle and merge into trimers of dimers at the hairpin tip (Figure S1). The MH1 helices in one subunit of each dimer interact at the trimer axis, but their counterparts at the trimer periphery have different partners and conceivably different functional roles (Cassidy et al. 2015, 2023; Kim et al. 1999; Yang et al. 2019). Together, one receptor contacts CheW and another the P5 domain of CheA to control kinase activity. The third trimer member occupies an “outboard” position (Figure S1), where it can contact a member of the hexameric CheW rings (Yang et al. 2019) that contribute to array cooperativity but are not essential for kinase activation or control (Pinas et al. 2022).

Although the conformational and dynamic behaviors that control CheA activity at the Tsr hairpin tip remain a

mystery, the kinase-ON receptor tip might need some dynamic behavior to enable CheA to move through its multi-step reaction cycle (Hathcock et al. 2023; Jun et al. 2020; Mello et al. 2018; Pan et al. 2017). Conversely, a static receptor tip might “freeze” CheA activity, possibly at any of several steps in its reaction cycle. Accordingly, we suggest that MH bundles in the *a-d* packing arrangement have sufficiently stable structures to convey destabilizing forces through the flexible bundle to the hairpin tip, thereby promoting CheA activity (Figure 7). It then follows that a dynamic, *x-da* MH bundle might have less structural influence on the flexible bundle, thus enabling the hairpin tip to adopt a more stable, static conformation that stops CheA activity (Figure 8).

The bundle distortion at the dynamic junction in the AlphaFold model of Tsr (Figure 6) resembles one in the crystal structure of Tm14 (Pollard et al. 2009). Pollard et al. suggested that structural asymmetry at this site, triggered by a chemoeffector stimulus or by adaptational modification changes, could be a way of propagating CheA-control signals to the receptor tip (Pollard et al. 2009). It seems likely that the dynamic junction distortion in Tsr is a hallmark of the kinase-ON state, whereas the serine-induced OFF state could have little or no stable distortion of the MH bundle owing to elevated dynamic behavior of the *x-da* arrangement. Conceivably, the loss of a rigid structural connection like the dynamic junction distortion between the MH bundle and hairpin tip allows the receptor tip to adopt a more stable structure. The flexible bundle and glycine hinge (Figure 8) probably play an important role in this transmission step (Alexander and Zhulin 2007; Coleman et al. 2005; Pedetta et al. 2017). In vivo crosslinking approaches like those in the present study could help to elucidate the structural nature of stimulus signals traversing this region of the Tsr molecule.

4 | MATERIALS AND METHODS

4.1 | Bacterial strains and plasmids

Strains used in this study were derivatives of *E. coli* K12 strain RP437 (Parkinson 1978). All carried extensive in-frame deletions of the MCP-family chemoreceptor genes (*tsr*, *tar*, *tap*, *trg*, *aer*) and five auxotrophic mutations (*his*, *leu*, *met*, *thi*, *thr*). Additional properties relevant to the study were: UU2610 (CheR^{B−}) (Zhou et al. 2011); UU2612 (CheR^{B+}) (Zhou et al. 2011); UU2567 (CheRBYZ[−]) (Lai and Parkinson 2014).

Plasmid derivatives of pACYC184 (Chang and Cohen 1978) used in the study were vector pKG116 (Buron-Barral et al. 2006) which confers chloramphenicol resistance and has a sodium salicylate-inducible cloning

site; FRET reporter plasmid pRZ30, a pKG116 derivative that expresses *cheY-yfp* and *cheZ-cfp* under salicylate control (Lai and Parkinson 2014); and pPA114, a pKG116 derivative that expresses wild-type *tsr* under salicylate control (Ames et al. 2002). Plasmid derivatives of pBR322 (Bolivar et al. 1977) used in the study were pRR48, which confers ampicillin resistance and has an isopropyl- β -D-thiogalactopyranoside (IPTG)-inducible cloning site (Studdert and Parkinson 2005), and pRR53, a pRR48 derivative that expresses wild-type *tsr* under IPTG control (Studdert and Parkinson 2005).

4.2 | Site-directed mutagenesis

Mutations were created in pRR53 and pPA114 by Quick-Change PCR mutagenesis (Ames and Parkinson 2018) and confirmed by sequencing.

4.3 | Growth media

Liquid bacterial cultures were grown in T broth (1% tryptone and 0.5% NaCl wt/vol) or L broth (T broth plus 5 g/L yeast extract). Transformations were plated on L plates (1% tryptone, 0.5% NaCl wt/vol, 5 g/L yeast extract, 15% agar) containing 100 μ g/mL ampicillin. Chemotaxis assays were performed on T swim plates (T broth plus 0.25% agar) containing 100 μ M IPTG to induce Tsr proteins to native levels and 50 μ g/mL ampicillin.

4.4 | Soft agar chemotaxis assays

UU2612 transformant colonies carrying mutant pRR53 derivatives were transferred with toothpicks to T swim plates and incubated at 32.5°C for 6–7 h.

4.5 | Quantifying intracellular levels of mutant Tsr proteins

Protein expression assays were performed in strain UU2610, as previously described (Ames et al. 2016).

4.6 | BMOE crosslinking assays

BMOE crosslinking assays were performed as previously described (Flack and Parkinson 2022). Briefly, strain UU2610 carrying pRR53 and/or pPA114 CYS-reporter derivatives were grown at 30°C in tryptone broth with appropriate antibiotic and inducer concentrations. Cells

were collected at mid-exponential phase by centrifugation, washed once, then resuspended in tethering buffer (Slocum and Parkinson 1985). Cell samples with or without 10 mM serine were incubated for 20 min at 30°C before addition of BMOE (Thermo Scientific) to a final concentration of 20–200 μ M. Reactions were incubated at 30°C and quenched at various times by addition of NEM (N-ethylmaleimide) to a final concentration of 10 mM. Samples were pelleted and resuspended in 2X Laemmli sample buffer (Laemmli 1970). Samples to be reduced were resuspended in 2X Laemmli sample buffer containing 175 mM DTT (dithiothreitol). Cell samples were boiled for 5–10 min and their lysates analyzed by SDS-PAGE with 8 or 9% acrylamide gels and Tsr bands visualized by immunoblotting with polyclonal rabbit antiserum.

4.7 | In vivo FRET-based kinase assays

The experimental protocol followed (Lai and Parkinson 2014) with hardware and data analyzed as described in (Sourjik et al. 2007). BMOE crosslinking FRET was performed as described (Flack and Parkinson 2022).

4.8 | Statistics

Statistical calculations were performed in Microsoft Excel (version 16.83 for Mac) using Student's *t* test. A *p*-value of <0.001 was indicated with three asterisks (***), values <0.01 with two asterisks (**), and values <0.05 with one asterisk (*).

4.9 | Protein structure models

Atomic coordinates for the wild-type Tsr dimer embedded in a lipid membrane were extracted from a model of the core receptor signaling unit (Cassidy et al. 2023). Tsr atomic distance measurements were carried out with PyMOL (version 2.5.5 for Mac) (Schrödinger software).

4.10 | AlphaFold 3 structural predictions

The wild-type Tsr amino acid sequence was submitted to the AlphaFold 2 (Jumper et al. 2021) and AlphaFold 3 (beta) (Abramson et al. 2024) servers and the resultant .cif files were converted to a .pdb format using PyMol (version 3.0.3 for Mac) (Schrödinger software). Crick angle deviations were determined using SamCC Turbo (Szczepaniak et al. 2021) by manually defining the

cytoplasmic bundle as N-helix residues 266–389 and C-helix residues 393–516. The assignment of α -da packing was made based on a Crick angle of $26^\circ \pm 5^\circ$ (Dunin-Horkawicz and Lupas 2010b).

AUTHOR CONTRIBUTIONS

Georgina I. Reyes: Conceptualization; methodology; formal analysis; writing – review and editing; investigation. **Caralyn E. Flack:** Conceptualization; methodology; formal analysis; writing – review and editing; investigation. **John S. Parkinson:** Funding acquisition; supervision; writing – original draft; formal analysis.

ACKNOWLEDGMENTS

Thanks to Brian Crane, Claudia Studdert, and Ady Vaknin for constructive comments on earlier drafts of the manuscript. This work was supported by research grant GM19559 (J.S.P.) from the National Institute of General Medical Sciences and by the Scott A. Lloyd Memorial Graduate Fellowship at the University of Utah (G.I.R.). The Protein-DNA Core Facility at the University of Utah receives support from National Cancer Institute grant CA42014 to the Huntsman Cancer Institute.

CONFLICT OF INTEREST STATEMENT

The authors declare no conflicts of interest.

DATA AVAILABILITY STATEMENT

All data used for this article are available directly in the article and in the associated Supporting Information.

ORCID

John S. Parkinson  <https://orcid.org/0000-0001-8788-7844>

REFERENCES

- Abramson J, Adler J, Dunger J, Evans R, Green T, Pritzel A, et al. Accurate structure prediction of biomolecular interactions with AlphaFold 3. *Nature*. 2024;630:493–500.
- Alexander RP, Zhulin IB. Evolutionary genomics reveals conserved structural determinants of signaling and adaptation in microbial chemoreceptors. *Proc Natl Acad Sci U S A*. 2007;104:2885–90.
- Ames P, Hunter S, Parkinson JS. Evidence for a helix-clutch mechanism of transmembrane signaling in a bacterial chemoreceptor. *J Mol Biol*. 2016;428:3776–88.
- Ames P, Parkinson JS. Constitutively signaling fragments of Tsr, the *Escherichia coli* serine chemoreceptor. *J Bacteriol*. 1994;176:6340–8.
- Ames P, Parkinson JS. All-codon mutagenesis for structure–function studies of chemotaxis signaling proteins. *Methods Mol Biol*. 2018;1729:79–85.
- Ames P, Studdert CA, Reiser RH, Parkinson JS. Collaborative signaling by mixed chemoreceptor teams in *Escherichia coli*. *Proc Natl Acad Sci U S A*. 2002;99:7060–5.
- Amin DN, Hazelbauer GL. Chemoreceptors in signalling complexes: shifted conformation and asymmetric coupling. *Mol Microbiol*. 2010a;78:1313–23.
- Amin DN, Hazelbauer GL. The chemoreceptor dimer is the unit of conformational coupling and transmembrane signaling. *J Bacteriol*. 2010b;192:1193–200.
- Bartelli NL, Hazelbauer GL. Differential backbone dynamics of companion helices in the extended helical coiled-coil domain of a bacterial chemoreceptor. *Protein Sci*. 2015;24:1764–76.
- Bartelli NL, Hazelbauer GL. Bacterial chemoreceptor dynamics: helical stability in the cytoplasmic domain varies with functional segment and adaptational modification. *J Mol Biol*. 2016;428:3789–804.
- Bass RB, Falke JJ. Detection of a conserved alpha-helix in the kinase-docking region of the aspartate receptor by cysteine and disulfide scanning. *J Biol Chem*. 1998;273:25006–14.
- Bass RB, Falke JJ. The aspartate receptor cytoplasmic domain: in situ chemical analysis of structure, mechanism and dynamics. *Structure*. 1999;7:829–40.
- Bi S, Sourjik V. Stimulus sensing and signal processing in bacterial chemotaxis. *Curr Opin Microbiol*. 2018;45:22–9.
- Bolivar F, Rodriguez RL, Greene PJ, Betlach MC, Heyneker HL, Boyer HW, et al. Construction and characterization of new cloning vehicles. *Gene*. 1977;2:95–113.
- Borkovich KA, Alex LA, Simon MI. Attenuation of sensory receptor signaling by covalent modification. *Proc Natl Acad Sci U S A*. 1992;89:6756–60.
- Boyd A, Simon MI. Multiple electrophoretic forms of methyl-accepting chemotaxis proteins generated by stimulus-elicited methylation in *Escherichia coli*. *J Bacteriol*. 1980;143:809–15.
- Buron-Barral M, Gosink KK, Parkinson JS. Loss- and gain-of-function mutations in the F1-HAMP region of the *Escherichia coli* aerotaxis transducer Aer. *J Bacteriol*. 2006;188:3477–86.
- Butler SL, Falke JJ. Cysteine and disulfide scanning reveals two amphiphilic helices in the linker region of the aspartate chemoreceptor. *Biochemistry*. 1998;37:10746–56.
- Cassidy CK, Himes BA, Alvarez FJ, Ma J, Zhao G, Perilla JR, et al. CryoEM and computer simulations reveal a novel kinase conformational switch in bacterial chemotaxis signaling. *eLife*. 2015;4:08419.
- Cassidy CK, Qin Z, Frosio T, Gosink K, Yang Z, Sansom MSP, et al. Structure of the native chemotaxis core signaling unit from phage E-protein lysed *E. coli* cells. *mBio*. 2023;14:e0079323.
- Chang ACY, Cohen SN. Construction and characterization of amplifiable multicopy DNA cloning vehicles derived from the p15A cryptic miniplasmid. *J Bacteriol*. 1978;134:1141–56.
- Chelsky D, Dahlquist FW. Structural studies of methyl-accepting chemotaxis proteins of *Escherichia coli*: evidence for multiple methylation sites. *Proc Natl Acad Sci U S A*. 1980;77:2434–8.
- Coleman MD, Bass RB, Mehan RS, Falke JJ. Conserved glycine residues in the cytoplasmic domain of the aspartate receptor play essential roles in kinase coupling and on–off switching. *Biochemistry*. 2005;44:7687–95.
- Colin R, Ni B, Laganenka L, Sourjik V. Multiple functions of flagellar motility and chemotaxis in bacterial physiology. *FEMS Microbiol Rev*. 2021;45:fuab038.
- Danielson MA, Bass RB, Falke JJ. Cysteine and disulfide scanning reveals a regulatory alpha-helix in the cytoplasmic domain of the aspartate receptor. *J Biol Chem*. 1997;272:32878–88.

- DeFranco AL, Koshland DE Jr. Multiple methylation in processing of sensory signals during bacterial chemotaxis. *Proc Natl Acad Sci U S A*. 1980;77:2429–33.
- Dunin-Horkawicz S, Lupas AN. Comprehensive analysis of HAMP domains: implications for transmembrane signal transduction. *J Mol Biol*. 2010a;397:1156–74.
- Dunin-Horkawicz S, Lupas AN. Measuring the conformational space of square four-helical bundles with the program samCC. *J Struct Biol*. 2010b;170:226–35.
- Dunten P, Koshland DE Jr. Tuning the responsiveness of a sensory receptor via covalent modification. *J Biol Chem*. 1991;266:1491–6.
- Engstrom P, Hazelbauer GL. Multiple methylation of methyl-accepting chemotaxis proteins during adaptation of *E. coli* to chemical stimuli. *Cell*. 1980;20:165–71.
- Ferris HU, Dunin-Horkawicz S, Mondéjar LG, Hulko M, Hantke K, Martin J, et al. The mechanisms of HAMP-mediated signaling in transmembrane receptors. *Structure*. 2011;19:378–85.
- Ferris HU, Zeth K, Hulko M, Dunin-Horkawicz S, Lupas AN. Axial helix rotation as a mechanism for signal regulation inferred from the crystallographic analysis of the *E. coli* serine chemoreceptor. *J Struct Biol*. 2014;186:349–56.
- Flack CE, Parkinson JS. A zipped-helix cap potentiates HAMP domain control of chemoreceptor signaling. *Proc Natl Acad Sci U S A*. 2018;115:E3519–28.
- Flack CE, Parkinson JS. Structural signatures of *Escherichia coli* chemoreceptor signaling states revealed by cellular crosslinking. *Proc Natl Acad Sci U S A*. 2022;119:e2204161119.
- Gao Q, Cheng A, Parkinson JS. Conformational shifts in a chemoreceptor helical hairpin control kinase signaling in *Escherichia coli*. *Proc Natl Acad Sci U S A*. 2019;116:15651–60.
- Gordon JB, Hoffman MC, Troiano JM, Li M, Hazelbauer GL, Schlau-Cohen GS. Concerted differential changes of helical dynamics and packing upon ligand occupancy in a bacterial chemoreceptor. *ACS Chem Biol*. 2021;16:2472–80.
- Greenswag AR, Li X, Borbat PP, Samanta D, Watts KJ, Freed JH, et al. Preformed soluble chemoreceptor trimers that mimic cellular assembly states and activate CheA autophosphorylation. *Biochemistry*. 2015;54:3454–68.
- Han XS, Parkinson JS. An unorthodox sensory adaptation site in the *Escherichia coli* serine chemoreceptor. *J Bacteriol*. 2014;196:641–9.
- Hathcock D, Yu Q, Mello BA, Amin DN, Hazelbauer GL, Tu Y. A nonequilibrium allosteric model for receptor-kinase complexes: the role of energy dissipation in chemotaxis signaling. *Proc Natl Acad Sci U S A*. 2023;120:e2303115120.
- Hughson AG, Hazelbauer GL. Detecting the conformational change of transmembrane signaling in a bacterial chemoreceptor by measuring effects on disulfide cross-linking in vivo. *Proc Natl Acad Sci U S A*. 1996;93:11546–51.
- Hulko M, Berndt F, Gruber M, Linder JU, Truffault V, Schultz A, et al. The HAMP domain structure implies helix rotation in transmembrane signaling. *Cell*. 2006;126:929–40.
- Iwama T, Homma M, Kawagishi I. Uncoupling of ligand-binding affinity of the bacterial serine chemoreceptor from methylation- and temperature-modulated signaling states. *J Biol Chem*. 1997;272:13810–5.
- Jumper J, Evans R, Pritzel A, Green T, Figurnov M, Ronneberger O, et al. Highly accurate protein structure prediction with AlphaFold. *Nature*. 2021;596:583–9.
- Jun SY, Pan W, Hazelbauer GL. ATP binding as a key target for control of the chemotaxis kinase. *J Bacteriol*. 2020;202:e00095–20.
- Kashefi M, Malik N, Struppe JO, Thompson LK. Carbon-nitrogen REDOR to identify ms-timescale mobility in proteins. *J Magn Reson*. 2019;305:5–15.
- Kashefi M, Thompson LK. Signaling-related mobility changes in bacterial chemotaxis receptors revealed by solid-state NMR. *J Phys Chem B*. 2017;121:8693–705.
- Kim KK, Yokota H, Kim SH. Four-helical-bundle structure of the cytoplasmic domain of a serine chemotaxis receptor. *Nature*. 1999;400:787–92.
- Kitanovic S, Ames P, Parkinson JS. Mutational analysis of the control cable that mediates transmembrane signaling in the *E. coli* serine chemoreceptor. *J Bacteriol*. 2011;193:5062–72.
- Kitanovic S, Ames P, Parkinson JS. A trigger residue for transmembrane signaling in the *Escherichia coli* serine chemoreceptor. *J Bacteriol*. 2015;197:2568–79.
- Koshy SS, Eyles SJ, Weis RM, Thompson LK. Hydrogen exchange mass spectrometry of functional membrane-bound chemotaxis receptor complexes. *Biochemistry*. 2013;52:8833–42.
- Laemmli UK. Cleavage of structural proteins during the assembly of the head of bacteriophage T4. *Nature*. 1970;227:680–5.
- Lai RZ, Gosink KK, Parkinson JS. Signaling consequences of structural lesions that alter the stability of chemoreceptor dimers. *J Mol Biol*. 2017;429:823–35.
- Lai RZ, Parkinson JS. Functional suppression of HAMP domain signaling defects in the *E. coli* serine chemoreceptor. *J Mol Biol*. 2014;426:3642–55.
- Le Moual H, Quang T, Koshland DE Jr. Conformational changes in the cytoplasmic domain of the *Escherichia coli* aspartate receptor upon adaptive methylation. *Biochemistry*. 1998;37:14852–9.
- Levit MN, Stock JB. Receptor methylation controls the magnitude of stimulus–response coupling in bacterial chemotaxis. *J Biol Chem*. 2002;277:36760–5.
- Li M, Hazelbauer GL. Core unit of chemotaxis signaling complexes. *Proc Natl Acad Sci U S A*. 2011;108:9390–5.
- Li X, Eyles SJ, Thompson LK. Hydrogen exchange of chemoreceptors in functional complexes suggests protein stabilization mediates long-range allosteric coupling. *J Biol Chem*. 2019;294:16062–79.
- Lin LN, Li J, Brandts JF, Weis RM. The serine receptor of bacterial chemotaxis exhibits half-site saturation for serine binding. *Biochemistry*. 1994;33:6564–70.
- Lupas AN, Gruber M. The structure of alpha-helical coiled coils. *Adv Protein Chem*. 2005;70:37–78.
- Malik N, Wahlbeck KA, Thompson LK. Strategies for identifying dynamic regions in protein complexes: flexibility changes accompany methylation in chemotaxis receptor signaling states. *Biochim Biophys Acta Biomembr*. 2020;1862:183312.
- Massazza DA, Parkinson JS, Studdert CA. Cross-linking evidence for motional constraints within chemoreceptor trimers of dimers. *Biochemistry*. 2011;50:820–7.
- Mello BA, Pan W, Hazelbauer GL, Tu Y. A dual regulation mechanism of histidine kinase CheA identified by combining network-dynamics modeling and system-level input–output data. *PLoS Comput Biol*. 2018;14:e1006305.
- Pan W, Dahlquist FW, Hazelbauer GL. Signaling complexes control the chemotaxis kinase by altering its apparent rate constant of autophosphorylation. *Protein Sci*. 2017;26:1535–46.

- Parkinson JS. Complementation analysis and deletion mapping of *Escherichia coli* mutants defective in chemotaxis. *J Bacteriol.* 1978;135:45–53.
- Parkinson JS. Signaling mechanisms of HAMP domains in chemoreceptors and sensor kinases. *Annu Rev Microbiol.* 2010;64:101–22.
- Parkinson JS, Hazelbauer GL, Falke JJ. Signaling and sensory adaptation in *Escherichia coli* chemoreceptors: 2015 update. *Trends Microbiol.* 2015;23:257–66.
- Pedetta A, Massazza DA, Herrera Seitz MK, Studdert CA. Mutational replacements at the “glycine hinge” of the *Escherichia coli* chemoreceptor Tsr support a signaling role for the C-helix residue. *Biochemistry.* 2017;56:3850–62.
- Pedetta A, Parkinson JS, Studdert CA. Signalling-dependent interactions between the kinase-coupling protein CheW and chemoreceptors in living cells. *Mol Microbiol.* 2014;93:1144–55.
- Pinas GE, DeSantis MD, Cassidy CK, Parkinson JS. Hexameric rings of the scaffolding protein CheW enhance response sensitivity and cooperativity in *Escherichia coli* chemoreceptor arrays. *Sci Signal.* 2022;15:eabj1737.
- Pinas GE, Frank V, Vaknin A, Parkinson JS. The source of high signal cooperativity in bacterial chemosensory arrays. *Proc Natl Acad Sci U S A.* 2016;113:3335–40.
- Pollard AM, Bilwes AM, Crane BR. The structure of a soluble chemoreceptor suggests a mechanism for propagating conformational signals. *Biochemistry.* 2009;48:1936–44.
- Rice MS, Dahlquist FW. Sites of deamidation and methylation in Tsr, a bacterial chemotaxis sensory transducer. *J Biol Chem.* 1991;266:9746–53.
- Samanta D, Borbat PP, Dzikovski B, Freed JH, Crane BR. Bacterial chemoreceptor dynamics correlate with activity state and are coupled over long distances. *Proc Natl Acad Sci U S A.* 2015;112:2455–60.
- Scheinost JC, Gligoris TG. Structurally guided in vivo crosslinking. *Methods Mol Biol.* 2018;1764:123–32.
- Sherris D, Parkinson JS. Posttranslational processing of methyl-accepting chemotaxis proteins in *Escherichia coli*. *Proc Natl Acad Sci U S A.* 1981;78:6051–5.
- Slocum MK, Parkinson JS. Genetics of methyl-accepting chemotaxis proteins in *Escherichia coli*: null phenotypes of the *tar* and *tap* genes. *J Bacteriol.* 1985;163:586–94.
- Sourjik V, Berg HC. Receptor sensitivity in bacterial chemotaxis. *Proc Natl Acad Sci U S A.* 2002;99:123–7.
- Sourjik V, Vaknin A, Shimizu TS, Berg HC. In vivo measurement by FRET of pathway activity in bacterial chemotaxis. *Methods Enzymol.* 2007;423:365–91.
- Starrett DJ, Falke JJ. Adaptation mechanism of the aspartate receptor: electrostatics of the adaptation subdomain play a key role in modulating kinase activity. *Biochemistry.* 2005;44:1550–60.
- Studdert CA, Parkinson JS. Crosslinking snapshots of bacterial chemoreceptor squads. *Proc Natl Acad Sci U S A.* 2004;101:2117–22.
- Studdert CA, Parkinson JS. Insights into the organization and dynamics of bacterial chemoreceptor clusters through in vivo crosslinking studies. *Proc Natl Acad Sci U S A.* 2005;102:15623–8.
- Swain KE, Falke JJ. Structure of the conserved HAMP domain in an intact, membrane-bound chemoreceptor: a disulfide mapping study. *Biochemistry.* 2007;46:13684–95.
- Swain KE, Gonzalez MA, Falke JJ. Engineered socket study of signaling through a four-helix bundle: evidence for a yin-yang mechanism in the kinase control module of the aspartate receptor. *Biochemistry.* 2009;48:9266–77.
- Szczepaniak K, Bukala A, da Silva Neto AM, Ludwiczak J, Dunin-Horkawicz S. A library of coiled-coil domains: from regular bundles to peculiar twists. *Bioinformatics.* 2021;36:5368–76.
- Watts KJ, Johnson MS, Taylor BL. Different conformations of the kinase-on and kinase-off signaling states in the Aer HAMP domain. *J Bacteriol.* 2011;193:4095–103.
- Winston SE, Mehan R, Falke JJ. Evidence that the adaptation region of the aspartate receptor is a dynamic four-helix bundle: cysteine and disulfide scanning studies. *Biochemistry.* 2005;44:12655–66.
- Wuichet K, Zhulin IB. Origins and diversification of a complex signal transduction system in prokaryotes. *Sci Signal.* 2010;3:ra50.
- Yang W, Cassidy CK, Ames P, Diebold CA, Schulten K, Luthey-Schulten Z, et al. In situ conformational changes of the *Escherichia coli* serine chemoreceptor in different signaling states. *mBio.* 2019;10:e00973-19.
- Zhou Q, Ames P, Parkinson JS. Mutational analyses of HAMP helices suggest a dynamic bundle model of input–output signalling in chemoreceptors. *Mol Microbiol.* 2009;73:801–14.
- Zhou Q, Ames P, Parkinson JS. Biphasic control logic of HAMP domain signalling in the *Escherichia coli* serine chemoreceptor. *Mol Microbiol.* 2011;80:596–611.

SUPPORTING INFORMATION

Additional supporting information can be found online in the Supporting Information section at the end of this article.

How to cite this article: Reyes GI, Flack CE, Parkinson JS. The structural logic of dynamic signaling in the *Escherichia coli* serine chemoreceptor. *Protein Science.* 2024;33(12):e5209. <https://doi.org/10.1002/pro.5209>

Supplementary Information for

The Structural Logic of Dynamic Signaling in the *Escherichia coli* Serine Chemoreceptor

Georgina I. Reyes, Caralyn E. Flack and John S. Parkinson*

John S. Parkinson

E-mail: parkinson@biology.utah.edu

This file includes:

Figures S1 - S8

Tables S1-S2

SI references

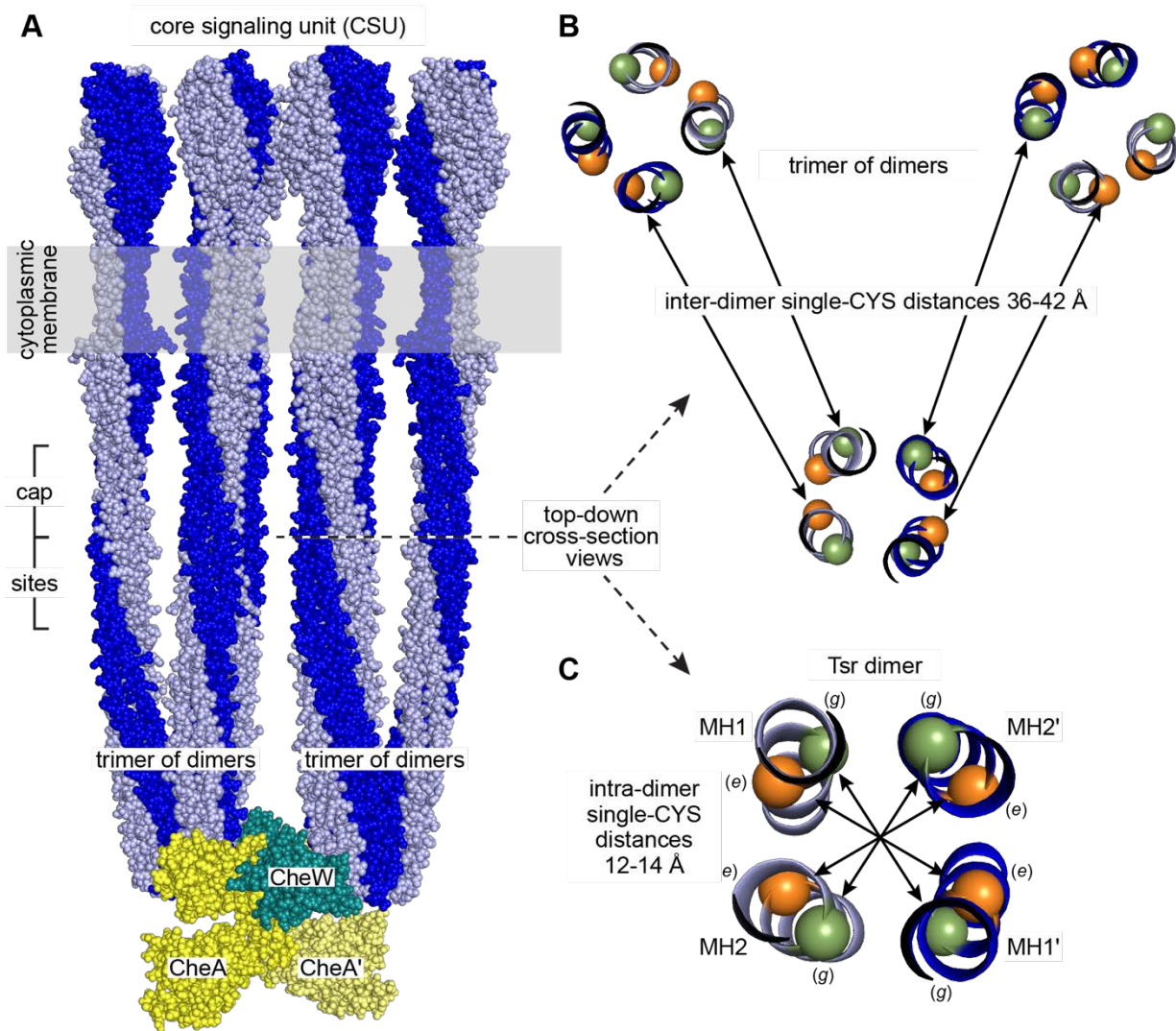


Fig. S1. Distances between single-cysteine (CYS) reporter sites in Tsr dimers and trimers of dimers. (A) Membrane-embedded Tsr core signaling unit (CSU); atomic coordinates from PDB: 8C5V (1). The CSU contains six Tsr dimers (light and dark blue subunits) organized in two trimers of dimers, one CheA dimer and two CheW proteins, one of which is largely hidden behind the receptors. (B) Top-down cross-section of a Tsr trimer showing one-heptad slabs of the three dimers at the cap-sites junction of the MH bundle. Spheres are alpha-carbon atoms of the *e* (orange) and *g* (green) edge residues that flank the packing faces of the 4-helix bundles. Closest inter-dimer distances between single-CYS reporter sites were determined with PyMol 2.5.5 (Shrödinger software). (Note that the distances between the beta-carbons of cysteine residues at those reporter sites would be several Å less.) (C) Top-down cross-section view of the reporter sites in an individual receptor dimer. Distances between the single-CYS sites within the dimer were measured with PyMol. (Note that the distances between the beta-carbons of cysteine residues at the reporter sites would be several Å less.)

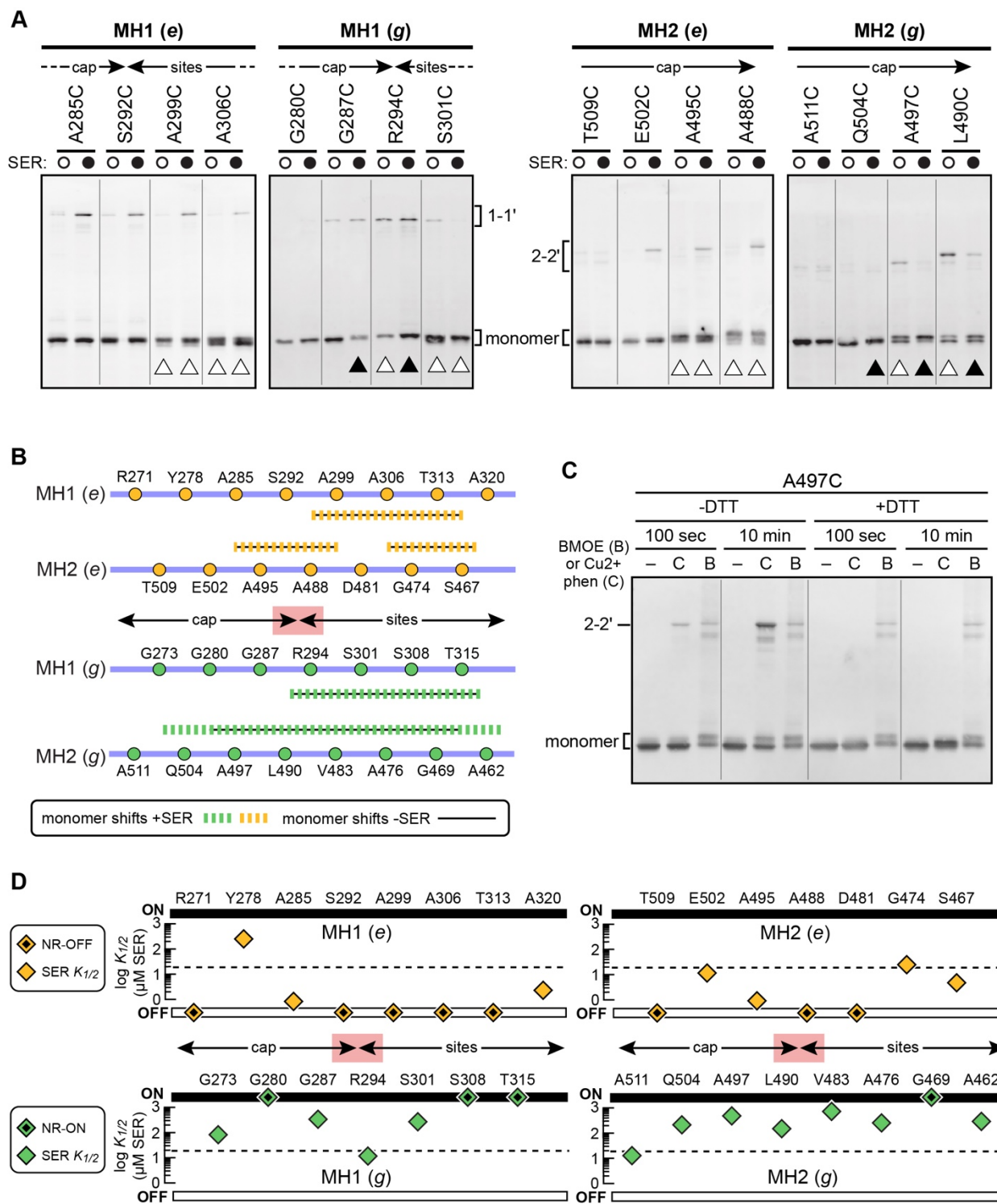


Fig. S2. Tsr single-CYS crosslinking data. Legend is on following page.

Fig. S2. Tsr single-CYS crosslinking data.

(A) Examples of single-CYS crosslinking gels. UU2610 cells carrying single-CYS reporter plasmids in the presence (black circles) or absence (white circles) of 10 mM serine were treated with 200 μ M BMOE for 100 seconds at 30°C. Triangles indicate reporters that produced shifted monomer bands. Black triangles indicate reporters that produced a greater fraction of shifted subunits in the presence of serine. All panels show the MH bundle regions where adjacent reporters transitioned from no monomer shifts to readily apparent monomer shifts.

(B) Summary of MH bundle dynamic behaviors inferred from BMOE-induced mobility shifts of single-CYS receptor subunits. Broken lines indicate regions in which reporters produced shifted monomer bands in the presence of serine; black lines indicate bandshift effects seen in the absence of serine. The red rectangle at the cap-sites border is the dynamic junction defined in Fig. 2.

(C) Modifications of A497C monomers induced by BMOE and Cu²⁺ phenanthroline. UU2610 cells carrying a Tsr-A497C derivative of plasmid pRR53 were treated at 30°C with no crosslinker (–), 200 μ M BMOE or 300 μ M Cu²⁺ phenanthroline for either 100 seconds or 10 minutes. All cells were pre-treated with 10 mM serine to enhance monomer bandshifts. Sample aliquots were treated with 175 mM dithiothreitol (+DTT) to reduce disulfide bonds before SDS-PAGE analysis.

(D) FRET kinase control properties of uncrosslinked Tsr single-CYS reporters. UU2567 cells carrying Tsr expression plasmid pRR53 single-CYS derivatives were tested for serine responses in FRET kinase assays (see Methods for experimental details). NR-OFF receptors exhibited no response to serine stimuli up to 10 mM and no FRET change in response to 3 mM KCN, indicative of no CheA activity. NR-ON receptors exhibited kinase activity upon KCN challenge but failed to inhibit that activity when challenged with 10 mM serine. The dashed horizontal lines indicate the $K_{1/2}$ serine response value for wild-type Tsr. The red rectangle at the cap-sites border is the dynamic junction defined in Fig. 2.

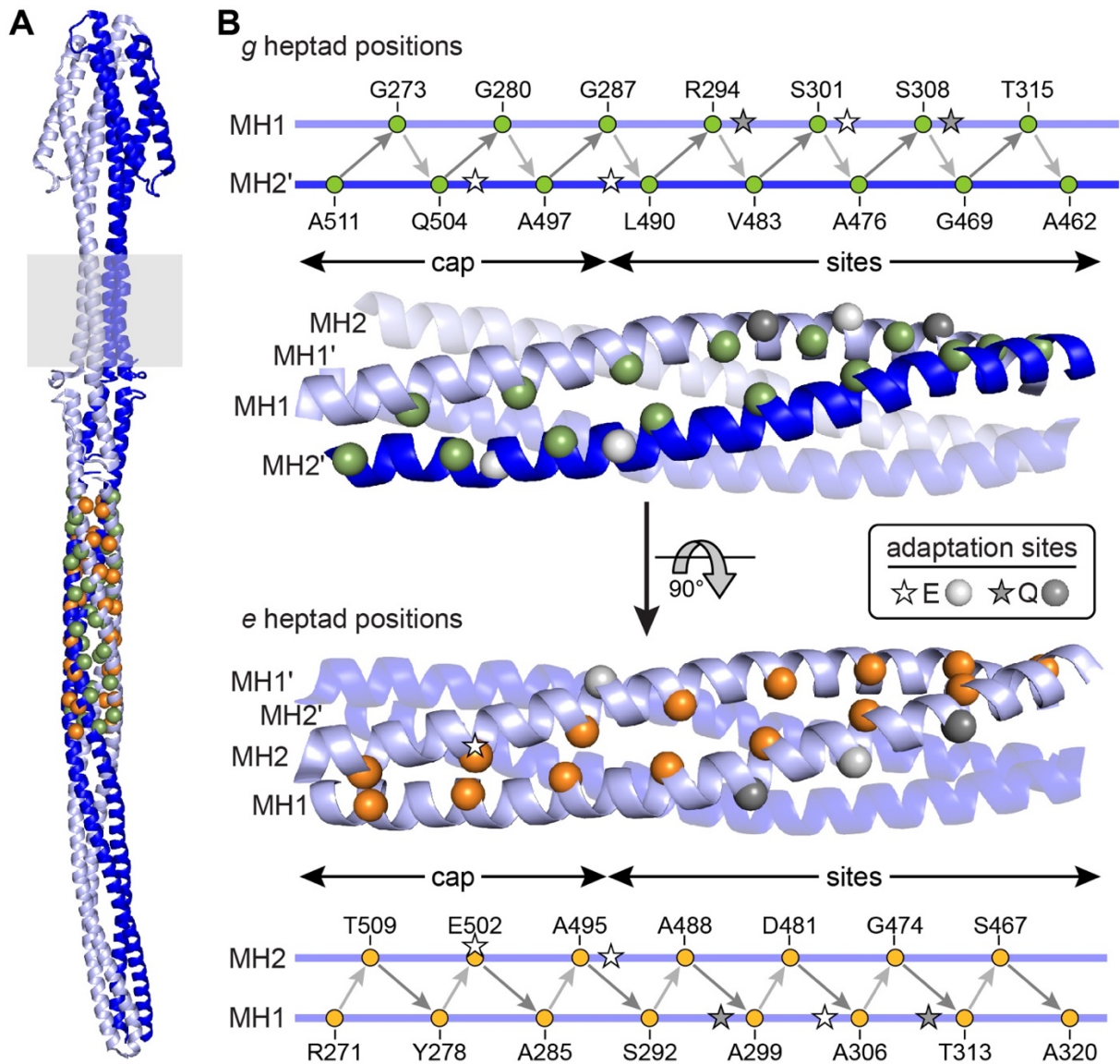


Fig. S3. Structural arrangements of cysteine reporter sites at bundle edge residues.

(A) A full-length membrane-embedded Tsr dimer; atomic coordinates were extracted from PDB: 8C5V (1) and analyzed with PyMol 2.5.5 (Schrödinger software). The two subunits are in different shades of blue and the membrane is depicted by a gray rectangle. The alpha-carbons of the MH bundle *e* (orange) and *g* (green) edge residues are indicated by spheres, which are shown at 1.5X scale to enhance their visibility.

(B) The positions of cysteine reporter sites are shown on the helix backbone structures and labeled in the accompanying cartoons (in which the relative positions of reporter sites are only approximate). Only one set of reporter site atoms is shown for the dimer, with the two helices in back dimmed. Distances between alpha carbons of adjacent reporter sites were measured with PyMol 2.5.5 (Schrödinger software) for the two CYS-pairs at each position in the dimer. (Note that the distances between beta-carbons of cysteine residues at the reporter sites would be several Å less.) Distances between adjacent *g*-CYS sites in the MH2'-MH1 direction (dark gray arrows) had a composite average and standard deviation of 10.2 ± 0.7 Å; corresponding values for sites in the MH1-MH2' direction (light gray arrows) were 6.6 ± 0.5 Å. Distances between *e*-CYS sites in the MH1-MH2 direction (light gray arrows) averaged 6.3 ± 0.9 Å; distances between sites in the MH2-MH1 direction (dark gray arrows) were 9.4 ± 0.6 Å.

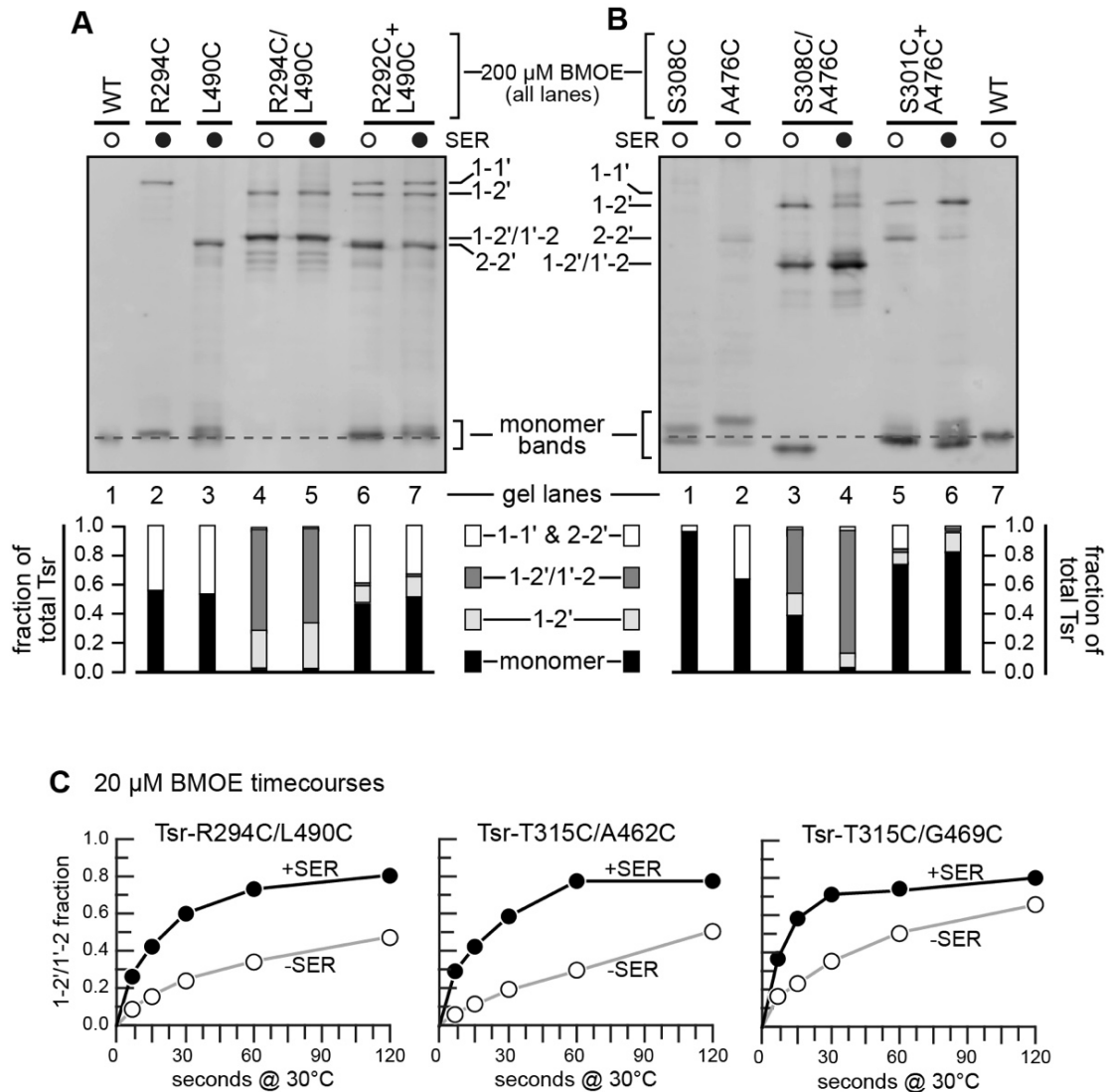


Fig. S4. Examples of Tsr *g/g* crosslinking data.

(A and B) Crosslinking reactions with 200 μM BMOE that illustrate the controls and logic used to identify the 1-2'/1'-2 crosslinking products. The dashed horizontal line marks the position of wild-type Tsr subunits (no CYS reporters). Note that uncrosslinked single-CYS reporter subunits may migrate slightly slower (A2; A3) or faster (B1; B2) than wild-type monomers. Such effects can be due to an intrinsic shift in subunit mobility and/or to a BMOE-induced modification (see Fig. S2), but have little effect on the relative positions of dimer-sized crosslinking products. The dimer bands in the single-CYS control lanes identify the 1-1' and 2-2' products. If not readily visible at the exposures that detect the 1-2' and 1-2'/1'-2 products (e.g., B1; B2), a longer exposure image (not shown) was used to ascertain the 1-1' and 2-2' band positions. Co-expression of two single-CYS receptors from compatible plasmid vectors in the same cell produces a third band that identifies the 1-2' crosslinked species (A6, A7; B5, B6). The CYS-pair reporters reveal a fourth band that is the doubly-crosslinked 1-2'/1'-2 product (A4, A5; B3, B4). The additional bands in lanes A4 -A7, B3-4 most likely represent degradation products of the predominant 1-2' and 1-2'/1'-2 species that are produced by periplasmic proteases upon lysis of the cell samples. (Note that a single cleavage site in the protomer could create up to four distinct cleavage products.) Those bands were not seen in all experiments and were not included in the band quantifications shown in the stacked histograms below the gels.

(C) Timecourses of crosslinking reactions with 20 μM BMOE reveal a serine-promoted increase in crosslinking that was not evident in 200 μM BMOE reactions with these reporter pairs (see Fig. 3).

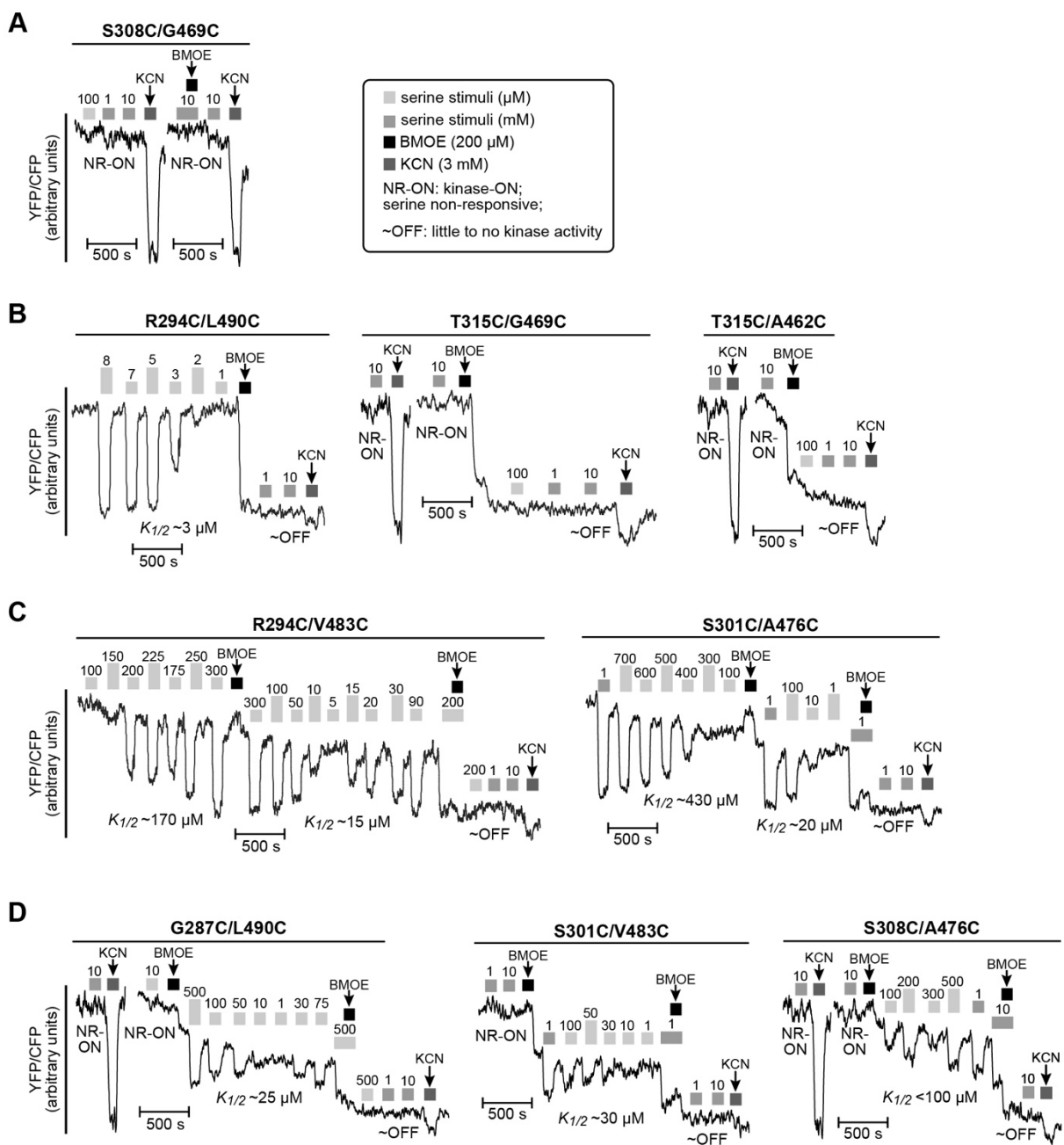


Fig. S6. FRET kinase assays of Tsr *g/g* reporters before and after BMOE treatment. FRET values (YFP/CFP) reflect CheA kinase activity; all plots are shown at the same scale. Small FRET drops produced by KCN treatments in the absence of CheA activity are probably due to differential effects of cellular pH changes on YFP and CFP emission efficiencies (2).

(A) Example of a serine non-responsive (NR), kinase-ON receptor; no BMOE effect.

(B) Examples of kinase-ON, serine-responsive receptors that lose kinase activity upon BMOE treatment.

(C) Examples of kinase-ON, serine-responsive receptors that become more serine-sensitive upon a first BMOE treatment, then lose all kinase activity upon a second BMOE treatment in conjunction with a saturating serine stimulus.

(D) Examples of kinase-ON, but non-responsive receptors whose kinase activity becomes serine-sensitive following an initial BMOE treatment, then becomes kinase-OFF after a second BMOE treatment in conjunction with a saturating serine stimulus.

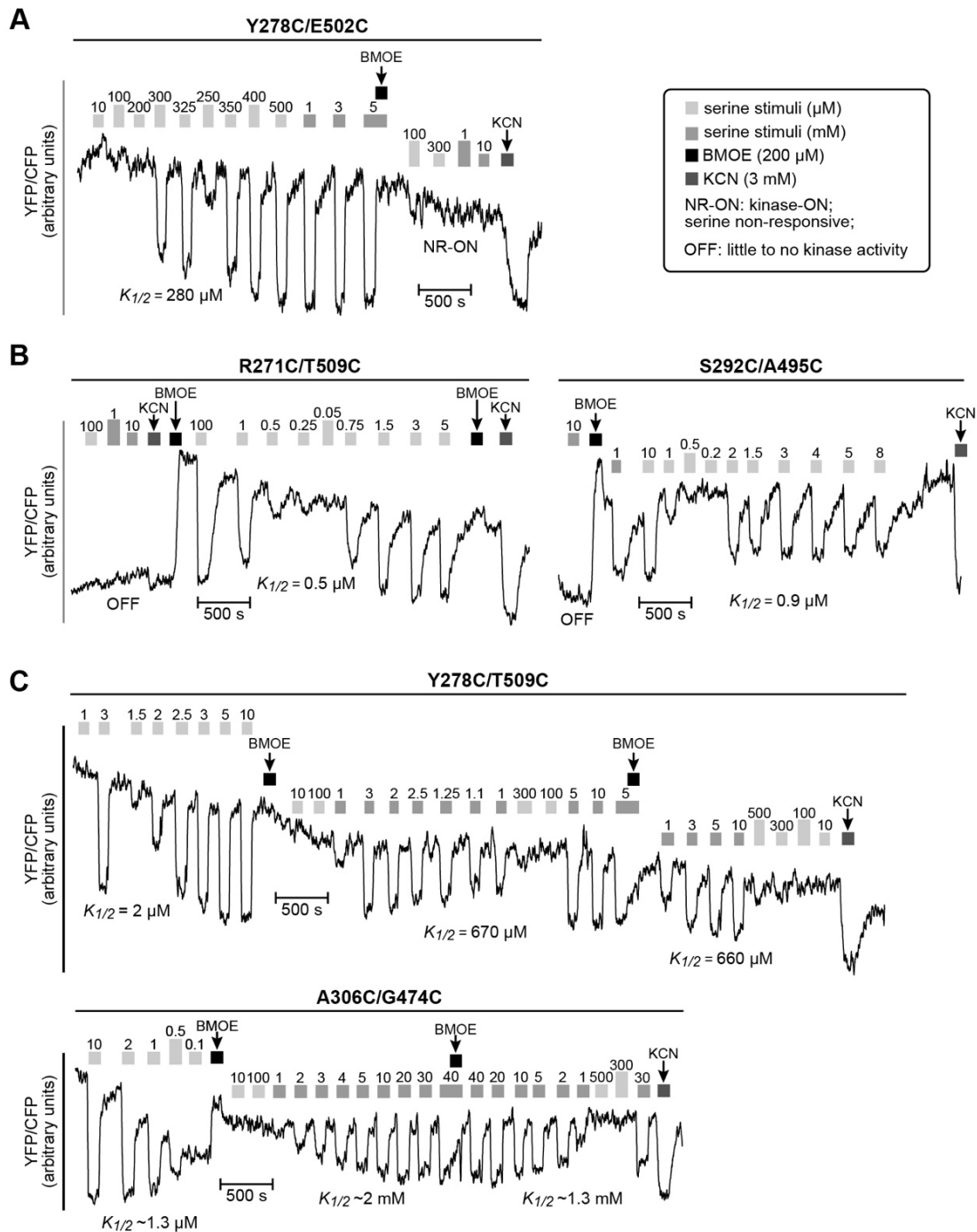


Fig. S7. FRET kinase assays of Tsr *e/e* reporters before and after BMOE treatment. FRET values (YFP/CFP) reflect CheA kinase activity; all plots are shown at the same scale. (A) Example of a kinase-active, serine-responsive receptor; BMOE treatment locks kinase activity in the ON state. (B) Examples of kinase-OFF receptors that become kinase active and serine-responsive upon BMOE treatment. (C) Examples of kinase-active, serine-responsive receptors that become less serine-sensitive upon BMOE treatment. A second BMOE treatment in conjunction with a saturating serine stimulus produces little change in serine sensitivity. The A306C/G474C receptor lost kinase activity upon repeated serine stimuli but became kinase-active and serine-responsive again after BMOE treatment, with no further loss of kinase activity or change in serine sensitivity.

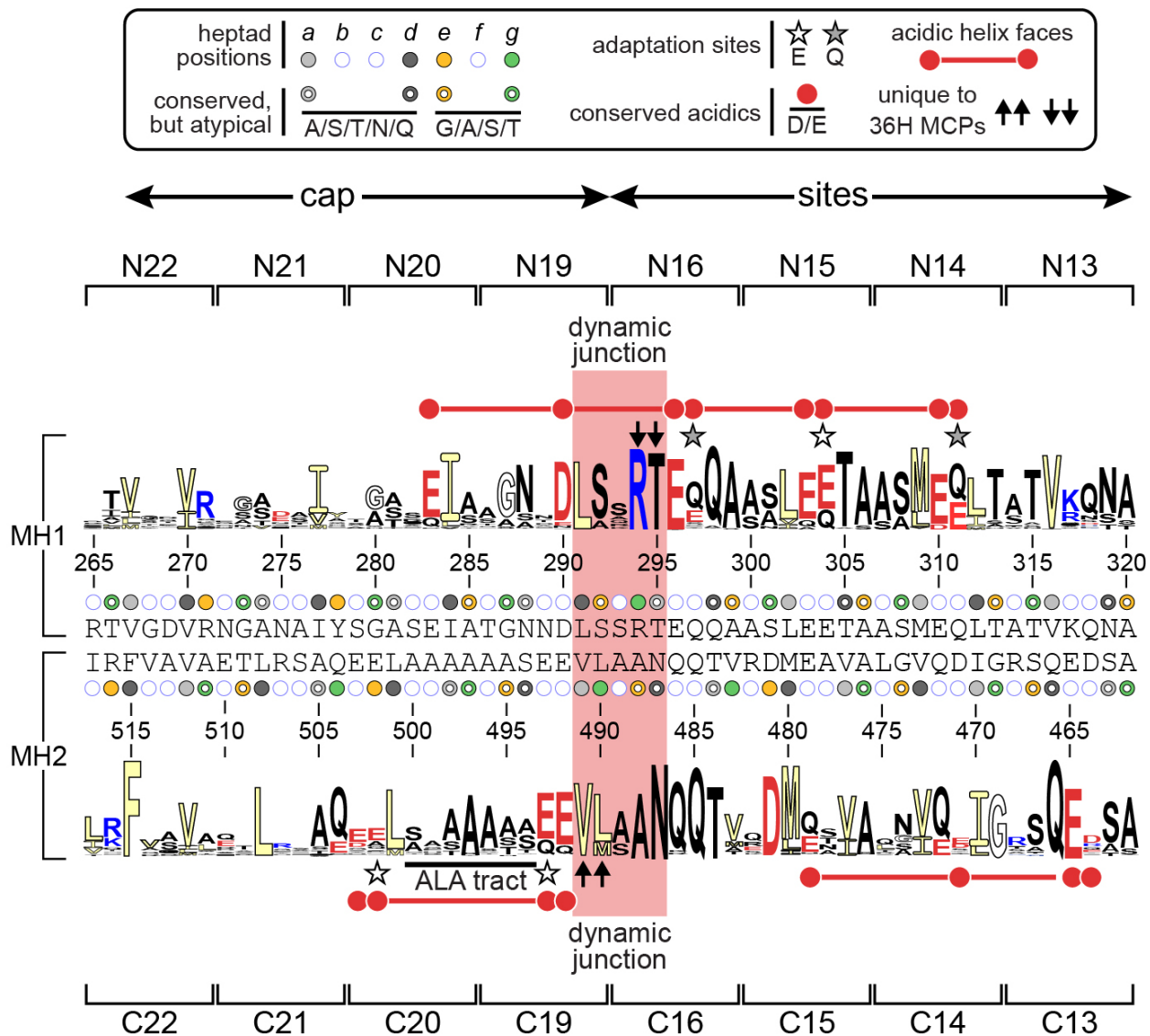


Fig. S8. Conserved residues and structural features of the Tsr MH bundle. The sequence logo (3) depicts the predominant residues at each MH bundle position in 2,428 nonredundant members (4) of the 36H class of chemoreceptors (5). Tsr residues and keyed heptad positions are listed between the MH1 and MH2 logos. The segment with a red background is the dynamic junction identified in this study.

Table S1. Functional properties of Tsr CYS reporters (in pRR53 plasmid derivatives).

<i>g</i> -heptad reporters				
<i>g</i> -CYS residue	function ^a	amount ^b	$K_{1/2}$ (μ M SER) ^c	CheA activity ^d
MH1				
G273C	0.95	1.4	74	1.1
G280C	1.2	0.75	NR-ON	1.0
G287C	0.90	1.3	330	0.80
R294C	0.20	0.95	14	1.4
S301C	0.75	0.65	270	0.85
S308C	1.2	2.0	NR-ON	0.75
T315C	0.80	1.9	NR-ON	1.0
MH2				
A511C	0.85	1.1	12	0.75
Q504C	0.90	1.5	140	1.3
A497C	1.0	1.7	430	1.2
L490C	0.85	0.70	130	1.4
V483C	0.90	1.4	740	1.4
A476C	0.60	0.80	240	0.85
G469C	0.15	0.50	NR-ON	0.85
A462C	0.45	1.5	250	1.2
<i>g/g</i> reporter pairs				
<i>g/g</i> CYS residues	function ^a	amount ^b	$K_{1/2}$ (μ M SER) ^c	CheA activity ^d
MH1/MH2				
G273C/A511C	0.60	0.75	97	0.90
G273C/Q504C	0.95	0.70	410	1.2
G280C/Q504C	0.55	0.75	NR-ON	1.6
G280C/A497C	0.15	0.80	NR-ON	1.1
G287C/A497C	0.50	1.2	347.10	0.70
G287C/L490C	0.55	1.1	NR-ON	0.75
R294C/L490C	0.20	0.65	3.0	1.6
R294C/V483C	0.30	0.80	170	1.4
S301C/V483C	0.80	1.2	NR-ON	0.50
S301C/A476C	0.25	0.60	480	0.60
S308C/A476C	0.20	0.50	NR-ON	1.2
S308C/G469C	0.15	0.85	NR-ON	1.3
T315C/G469C	0.15	0.65	NR-ON	1.3
T315C/A462C	0.50	1.6	NR-ON	1.3

e-heptad reporters				
e-CYS residue	function ^a	amount ^b	$K_{1/2}$ (μ M SER) ^c	CheA activity ^d
MH1				
R271C	0.10	0.85	NR-OFF	0.00
Y278C	0.65	0.85	310	0.85
A285C	0.45	1.2	0.90	1.3
S292C	0.20	0.85	NR-OFF	0.00
A299C	0.20	0.70	NR-OFF	0.00
A306C	0.30	0.60	NR-OFF	0.00
T313C	0.30	0.65	NR-OFF	0.00
A320C	0.10	0.65	2.1	1.3
MH2				
T509C	0.10	1.1	NR-OFF	0.00
E502C	0.65	1.1	16	1.3
A495C	0.60	1.9	NR-OFF	0.75
A488C	0.35	0.65	NR-OFF	0.00
D481C	0.10	0.75	NR-OFF	0.00
G474C	0.65	0.75	29	1.3
S467C	0.15	0.90	5.0	1.6

e/e reporter pairs				
e/e CYS residues	function ^a	amount ^b	$K_{1/2}$ (μ M SER) ^c	CheA activity ^d
MH1/MH2				
R271C/T509C	0.05	0.75	NR-OFF	0.00
Y278C/T509C	0.35	1.3	NR-OFF	1.2
Y278C/E502C	0.75	1.1	2.0	1.1
A285C/E502C	0.50	1.1	280	1.2
A285C/A495C	0.15	0.75	84	0.00
S292C/A495C	0.10	2.2	NR-OFF	0.00
S292C/A488C	0.10	1.8	NR-OFF	0.00
A299C/A488C	0.20	1.5	NR-OFF	0.00
A299C/D481C	0.10	2.6	NR-OFF	0.00
A306C/D481C	0.10	1.6	NR-OFF	0.00
A306C/G474C	0.50	1.0	1.4	0.85
T313C/G474C	0.65	1.2	3.4	1.8
T313C/S467C	0.15	2.1	1.0	1.3
A320C/S467C	0.70	1.5	18	1.4

^a Colony size relative to wild-type Tsr control on tryptone soft agar; pRR53 mutant plasmids in strain UU2612.

^b Amount of mutant protein relative to wild-type Tsr control; pRR53 mutant plasmids in strain UU2610.

^c FRET assay of pRR53 mutant plasmids in strain UU2567; NR-ON: activity, no SER response; NR-OFF: no activity, no SER response.

^d Activity relative to wild-type Tsr control in FRET assay of pRR53 mutant plasmids in strain UU2567.

All data rounded as follows: values <1 rounded to 0.05; values <10 rounded to 0.1; values <100 rounded to 1; values <1000 rounded to 10.

Table S2. Raw crosslinking data for Tsr CYS-pair reporters

1-2'/1'-2 fraction				
<i>g/g</i> -CYS pairs	-SER	+SER	N	p value
G273C/A511C	0.08 ± 0.02	0.37 ± 0.02	3	<0.001
G273C/Q504C	0.18 ± 0.02	0.70 ± 0.02	3	<0.001
G280C/Q504C	0.17 ± 0.02	0.78 ± 0.05	3	<0.001
G280C/A497C	0.17 ± 0.02	0.43 ± 0.02	3	<0.001
G287C/A497C	0.20 ± 0.02	0.55 ± 0.03	3	<0.001
G287C/L490C	0.34 ± 0.02	0.78 ± 0.02	5	<0.001
R294C/L490C	0.69 ± 0.09	0.70 ± 0.12	5	0.89
R294C/V483C	0.31 ± 0.04	0.67 ± 0.03	5	<0.001
S301C/V483C	0.55 ± 0.03	0.72 ± 0.03	5	0.002
S301C/A476C	0.43 ± 0.03	0.74 ± 0.03	5	<0.001
S308C/A476C	0.23 ± 0.04	0.74 ± 0.14	5	0.004
S308C/G469C	0.12 ± 0.04	0.53 ± 0.06	5	<0.001
T315C/G469C	0.82 ± 0.05	0.70 ± 0.13	5	0.21
T315C/A462C	0.83 ± 0.02	0.82 ± 0.04	5	0.66

1-2 + 1'-2' fraction				
<i>e/e</i> -CYS pairs	-SER	+SER	N	p value
R271C/T509C	0.15 ± 0.03	0.18 ± 0.05	3	0.40
Y278C/T509C	0.50 ± 0.11	0.28 ± 0.04	3	0.03
Y278C/E502C	0.60 ± 0.02	0.68 ± 0.11	3	0.27
A285C/E502C	0.46 ± 0.04	0.26 ± 0.02	3	0.001
A285C/A495C	0.16 ± 0.03	0.04 ± 0.01	3	0.002
S292C/A495C	0.18 ± 0.01	0.18 ± 0.03	3	0.74
S292C/A488C	0.06 ± 0.01	0.08 ± 0.01	3	0.015
A299C/A488C	0.06 ± 0.02	0.09 ± 0.03	3	0.24
A299C/D481C	0.15 ± 0.06	0.20 ± 0.01	3	0.21
A306C/D481C	0.21 ± 0.01	0.26 ± 0.03	3	0.03
A306C/G474C	0.32 ± 0.03	0.21 ± 0.05	3	0.03
T313C/G474C	0.43 ± 0.04	0.26 ± 0.07	3	0.02
T313C/S467C	0.53 ± 0.06	0.41 ± 0.06	3	0.08
A320C/S467C	0.23 ± 0.01	0.11 ± 0.03	3	0.002

Values in the -SER (no serine) and +SER (serine pre-treatment) columns are means ± standard deviations for N independent experiments; *p* values were determined by Student's t-test.

SI References

1. C. K. Cassidy *et al.*, Structure of the native chemotaxis core signaling unit from phage E-protein lysed *E. coli* cells. *mBio* **14**, e0079323 (2023).
2. H. Shinoda, M. Shannon, T. Nagai, Fluorescent proteins for investigating biological events in acidic environments. *Int J Mol Sci* **19** (2018).
3. G. E. Crooks, G. Hon, J. M. Chandonia, S. E. Brenner, WebLogo: a sequence logo generator. *Genome Res* **14**, 1188-1190 (2004).
4. A. Pedetta, D. A. Massazza, M. K. Herrera Seitz, C. A. Studdert, Mutational replacements at the "glycine hinge" of the *Escherichia coli* chemoreceptor Tsr support a signaling role for the C-Helix residue. *Biochemistry* **56**, 3850-3862 (2017).
5. R. P. Alexander, I. B. Zhulin, Evolutionary genomics reveals conserved structural determinants of signaling and adaptation in microbial chemoreceptors. *Proc. Natl. Acad. Sci. USA* **104**, 2885-2890 (2007).